

AD-A145 398

THERMOSONDE AND UHF RADAR MEASUREMENTS OF C2 SUB N AT 171
WESTFORD MASSACHUSETTS - JULY 1981(U) AIR FORCE
GEOPHYSICS LAB HANSCOM AFB MA J H BROWN ET AL.

UNCLASSIFIED

23 FEB 84 AFGL-TR-84-0109

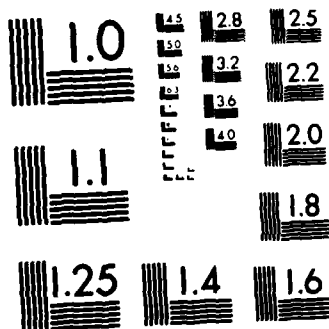
F/G 17/9

NL

END

THMEO

DTIC



MICROCOPY RESOLUTION TEST CHART
NATIONAL BUREAU OF STANDARDS 1963 A

12

AFGL-TR-84-0109
ENVIRONMENTAL RESEARCH PAPERS, NO. 876

Thermosonde and UHF Radar Measurements of C_n^2 at Westford, Massachusetts — July 1981

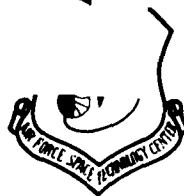
JAMES H. BROWN
ROBERT E. GOOD

23 February 1984

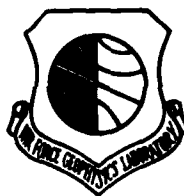
Approved for public release; distribution unlimited.



AD-A145 398



DTIC FILE COPY



OPTICAL PHYSICS DIVISION

AIR FORCE GEOPHYSICS LABORATORY

HANSCOM AFB, MA 01731

DTIC
ELECTE
SEP 13 1984
S D E


PROJECT 7670


84 09 12 004

This report has been reviewed by the ESD Public Affairs Office (PA) and is releasable to the National Technical Information Service (NTIS).

This technical report has been reviewed and is approved for publication.

FOR THE COMMANDER


ROBERT W. FENN
Branch Chief


JOHN S. GARING
Division Director

Qualified requestors may obtain additional copies from the Defense Technical Information Center.

If your address has changed, or if you wish to be removed from the mailing list, or if the addressee is no longer employed by your organization, please notify AFGL/DAA, Hanscom AFB, MA 01731. This will assist us in maintaining a current mailing list.

Do not return copies of this report unless contractual obligation or notices on a specific document requires that it be returned.

Unclassified

SECURITY CLASSIFICATION OF THIS PAGE

REPORT DOCUMENTATION PAGE				
1a. REPORT SECURITY CLASSIFICATION Unclassified		1b. RESTRICTIVE MARKINGS		
2a. SECURITY CLASSIFICATION AUTHORITY		3. DISTRIBUTION/AVAILABILITY OF REPORT Approved for public release; distribution unlimited.		
2b. DECLASSIFICATION/DOWNGRADING SCHEDULE				
4. PERFORMING ORGANIZATION REPORT NUMBER(S) AFGL-TR-84-0109 ERP, No. 876		5. MONITORING ORGANIZATION REPORT NUMBER(S)		
6a. NAME OF PERFORMING ORGANIZATION Air Force Geophysics Laboratory		6b. OFFICE SYMBOL (If applicable) OPA		7a. NAME OF MONITORING ORGANIZATION
6c. ADDRESS (City, State and ZIP Code) Hanscom AFB Massachusetts 01731		7b. ADDRESS (City, State and ZIP Code)		
8a. NAME OF FUNDING/SPONSORING ORGANIZATION		8b. OFFICE SYMBOL (If applicable)		9. PROCUREMENT INSTRUMENT IDENTIFICATION NUMBER
8c. ADDRESS (City, State and ZIP Code)		10. SOURCE OF FUNDING NOS.		
		PROGRAM ELEMENT NO. 62101F	PROJECT NO. 7670	TASK NO. 15 WORK UNIT NO. 07
11. TITLE (Include Security Classification) Thermosonde and UHF Radar Measurements of C_n^2 at Westford,				
12. PERSONAL AUTHOR(S) Massachusetts - July 1981 James H. Brown and Robert E. Good				
13a. TYPE OF REPORT Scientific. Interim.		13b. TIME COVERED FROM _____ TO _____		14. DATE OF REPORT (Yr., Mo., Day) 1984 February 23
15. PAGE COUNT 57				
16. SUPPLEMENTARY NOTATION <i>C_n n² guard</i>				
17. COSATI CODES			18. SUBJECT TERMS (Continue on reverse if necessary and identify by block number)	
FIELD	GROUP	SUB. GR.	Optical turbulence, Turbulence, C_n^2 , Refractive structure, Coherence, Isoplanatism, Radiosonde, Thermosonde, Scintillation	
19. ABSTRACT (Continue on reverse if necessary and identify by block number) → Five different instruments were used in coordinated multiple experiments to measure atmospheric turbulence. C_n^2 the optical refractive structure constant, was measured by thermosondes, UHF radar, stellar scintillometer, and aircraft mounted micro-thermal probes. Presented here are the results of 19 rawinsonde flights. Also comparisons of eight thermosonde/radar profiles, one radar, scintillometer, thermosonde profile, and several aircraft profiles are presented. For the scales discussed here, good agreement is shown between radar, thermosonde, and scintillometer data. Worse agreement is obtained from aircraft measurements. A diurnal shift in the C_n^2 profile is noted but no tropopause enhancement is found. <i>K</i>				
20. DISTRIBUTION/AVAILABILITY OF ABSTRACT UNCLASSIFIED/UNLIMITED <input type="checkbox"/> SAME AS RPT. <input checked="" type="checkbox"/> DTIC USERS <input type="checkbox"/>			21. ABSTRACT SECURITY CLASSIFICATION Unclassified	
22a. NAME OF RESPONSIBLE INDIVIDUAL James H. Brown			22b. TELEPHONE NUMBER (Include Area Code) (617) 861-5779	22c. OFFICE SYMBOL OPA

DD FORM 1473, 83 APR

EDITION OF 1 JAN 73 IS OBSOLETE.

Unclassified

SECURITY CLASSIFICATION OF THIS PAGE

Preface

The following individuals contributed toward data collection and reduction:

Telemetry	Mr. J. Griffin, LCR Mr. K. Walker, LCR
Radar observations	Dr. Brenton Watkins, Univ. of Alaska Mr. G. Lariot, NEROC
Scintillometer observations	Dr. A. Quesada, LKD
Data reduction	Ms. P. Bench, LKD Mr. B. Sullivan, Boston College Ms. D. Pelekasis, RMA Dr. B. Beland, Rio Grande Assoc. Mr. B. Bletsis, Rio Grande Assoc.
Theoretical discussions	Dr. E. Dewan, LKD

Accession For	
NTIS GRA&I	<input checked="checked" type="checkbox"/>
DTIC TAB	<input type="checkbox"/>
Unannounced	<input type="checkbox"/>
Justification	
Excluded from	
Distribution/	
Availability Codes	
Availability and/or	
Dist	Special
A-1	

Contents

1. INTRODUCTION	9
2. PROGRAM DESCRIPTION	10
3. THEORY	10
3.1 Thermosonde	10
3.2 Radar	11
3.3 Stellar Scintillometer	11
3.4 Aircraft Measurements	12
4. RAWINSONDE RESULTS	12
4.1 Temperature and Humidity	12
4.2 Wind Speed and Direction	13
4.3 Thermosonde C_n^2 Profiles - Hufnagel Comparisons	13
4.4 Averaged Thermosonde C_n^2 Profile	14
4.5 Coherence Scales	15
5. THERMOSONDE - RADAR COMPARISON	43
6. THERMOSONDE - RADAR-SCINTILLOMETER COMPARISON	48
7. THERMOSONDE - AIRCRAFT COMPARISON	49
REFERENCES	53
APPENDIX A: Solar Heating Effects on Probe Wire	55

Illustrations

1. Radiosonde Ambient Temperature and Relative Humidity Profiles - Flight QX0021	16
2. Radiosonde Ambient Temperature and Relative Humidity Profiles - Flight QX0024	16
3. Radiosonde Ambient Temperature and Relative Humidity Profiles - Flight QX0009	17
4. Radiosonde Ambient Temperature and Relative Humidity Profiles - Flight QX0050	17
5. Radiosonde Ambient Temperature and Relative Humidity Profiles - Flight QX0001	18
6. Radiosonde Ambient Temperature and Relative Humidity Profiles - Flight QX0008	18
7. Radiosonde Ambient Temperature and Relative Humidity Profiles - Flight QX0045	19
8. Radiosonde Ambient Temperature and Relative Humidity Profiles - Flight QX00007	19
9. Radiosonde Ambient Temperature and Relative Humidity Profiles - Flight QX0036	20
10. Radiosonde Ambient Temperature and Relative Humidity Profiles - Flight QX0012	20
11. Radiosonde Ambient Temperature and Relative Humidity Profiles - Flight QX0019	21
12. Radiosonde Ambient Temperature and Relative Humidity Profiles - Flight QX0038	21
13. Radiosonde Ambient Temperature and Relative Humidity Profiles - Flight QX0035	22
14. Radiosonde Ambient Temperature and Relative Humidity Profiles - Flight QX0043	22
15. Radiosonde Ambient Temperature and Relative Humidity Profiles - Flight QX0011	23
16. Radiosonde Ambient Temperature and Relative Humidity Profiles - Flight QX0034	23
17. Radiosonde Ambient Temperature and Relative Humidity Profiles - Flight QX0020	24
18. Radiosonde Ambient Temperature and Relative Humidity Profiles - Flight QX0040	24
19. Radiosonde Ambient Temperature and Relative Humidity Profiles - Flight QX0031	25
20. Winds Aloft Profile - Flight QX0024	25
21. Winds Aloft Profile - Flight QX0009	26
22. Winds Aloft Profile - Flight QX0050	26
23. Winds Aloft Profile - Flight QX0008	27
24. Winds Aloft Profile - Flight QX0045	27

Illustrations

25. Winds Aloft Profile - Flight QX0007	28
26. Winds Aloft Profile - Flight QX0036	28
27. Winds Aloft Profile - Flight QX0012	29
28. Winds Aloft Profile - Flight QX0019	29
29. Winds Aloft Profile - Flight QX0038	30
30. Winds Aloft Profile - Flight QX0035	30
31. Winds Aloft Profile - Flight QX0043	31
32. Winds Aloft Profile - Flight QX0011	31
33. Winds Aloft Profile - Flight QX0034	32
34. Winds Aloft Profile - Flight QX0020	32
35. Winds Aloft Profile - Flight QX0040	33
36. Winds Aloft Profile - Flight QX0031	33
37. Log-Average C_n^2 Thermosonde Profile and the Hufnagel Model - Flight QX0021	35
38. Log-Average C_n^2 Thermosonde Profile and the Hufnagel Model - Flight QX0024	35
39. Log-Average C_n^2 Thermosonde Profile and the Hufnagel Model - Flight QX0050	36
40. Log-Average C_n^2 Thermosonde Profile and the Hufnagel Model - Flight QX0045	36
41. Log-Average C_n^2 Thermosonde Profile and the Hufnagel Model - Flight QX0036	37
42. Log-Average C_n^2 Thermosonde Profile and the Hufnagel Model - Flight QX0012	37
43. Log-Average C_n^2 Thermosonde Profile and the Hufnagel Model - Flight QX0038	38
44. Log-Average C_n^2 Thermosonde Profile and the Hufnagel Model - Flight QX0035	38
45. Log-Average C_n^2 Thermosonde Profile and the Hufnagel Model - Flight QX0043	39
46. Log-Average C_n^2 Thermosonde Profile and the Hufnagel Model - Flight QX0011	39
47. Log-Average C_n^2 Thermosonde Profile and the Hufnagel Model - Flight QX0034	40
48. Log-Average C_n^2 Thermosonde Profile and the Hufnagel Model - Flight QX0020	40
49. Log-Average C_n^2 Thermosonde Profile and the Hufnagel Model - Flight QX0040	41
50. Log-Average C_n^2 Thermosonde Profile and the Hufnagel Model - Flight QX0031	41
51. Log-Average C_n^2 of Ten Daytime Thermosonde Flights	42

Illustrations

52.	Log-Average C_n^2 of Nine Nighttime Thermosonde Flights	42
53.	Normalized Difference Between Day and Night Measurements of $C_n^2 \equiv \left(\frac{\text{Day-Night}}{\text{Night}} \right)$	43
54.	Comparison of 500-m Log-Average Thermosonde Profiles and Composite Log-Average Radar Profiles - Flight QX0050	44
55.	Comparison of 500-m Log-Average Thermosonde Profiles and Composite Log-Average Radar Profiles - Flight QX0045	44
56.	Comparison of 500-m Log-Average Thermosonde Profiles and Composite Log-Average Radar Profiles - Flight QX0012	45
57.	Comparison of 500-m Log-Average Thermosonde Profiles and Composite Log-Average Radar Profiles - Flight QX0035	45
58.	Comparison of 500-m Log-Average Thermosonde Profiles and Composite Log-Average Radar Profiles - Flight QX0043	46
59.	Comparison of 500-m Log-Average Thermosonde Profiles and Composite Log-Average Radar Profiles - Flight QX0011	46
60.	Comparison of 500-m Log-Average Thermosonde Profiles and Composite Log-Average Radar Profiles - Flight QX0034	47
61.	Comparison of 500-m Log-Average Thermosonde Profiles and Composite Log-Average Radar Profiles - Flight QX0020	47
62.	Plot of Mean Differences Between Thermosonde and Radar C_n^2	48
63.	Comparisons Between Log-Average Thermosonde, Radar and Scintillometer C_n^2 Profiles - One Flight	49
64.	Thermosonde - Aircraft Profile (Ascent, Bridge No. 1)	50
65.	Thermosonde - Aircraft Profile (Descent, Bridge No. 1)	50
66.	Thermosonde - Aircraft Profile (Ascent, Bridge No. 2)	51
67.	Thermosonde - Aircraft Profile (Descent, Bridge No. 2)	51

Tables

1.	Balloon Flight Parameters	34
----	---------------------------	----

Thermosonde and UHF Radar Measurements of C_n^2 at Westford, Massachusetts - July 1981

1. INTRODUCTION

In July 1981 over 30 specialized AFGL radiosondes were launched from the Millstone Hill radar facility in Westford, Massachusetts.¹ The purpose was to provide turbulence data to determine the statistics of refractive index fluctuations and their influence on optical propagation degradation. The published data and models are insufficient to predict the role of turbulence and the extent turbulence degrades the performance of new communications, guidance and navigation systems. The particular objectives of these experiments were: (1) to expand the limited data base; (2) to compare the altitude profiles of C_n^2 from measurements by thermosonde, radar, aircraft, and stellar scintillometer; (3) to estimate an average C_n^2 profile for day and night conditions; and (4) to estimate coherence scales based on the thermosonde measurements.

(Received for publication 22 February 1984)

1. Brown, J. H., Good, R. E., Bench, P. M., and Faucher, G. E. (1982) Sonde Experiments for Comparative Measurements of Optical Turbulence, AFGL-TR-82-0079, AD A118740.

2. PROGRAM DESCRIPTION

Coordinated experiments were conducted near the Haystack observatory at Millstone Hill, Westford, Massachusetts from 10 February 1981 until 8 August 1981.¹ Turbulence was measured by AFGL modified radiosondes and thermosondes, the Northeast Radio Observatory Corporation (NEROC) 440 MHz UHF scatter radar, an AFWL stellar scintillometer, and a contractor instrumented aircraft. Personnel from the Northeast Radio Observatory Corporation operated the radar. The aircraft mounted micro-thermal probe measurements were provided by Airborne Research Associates, Bedford, Massachusetts. AFGL personnel launched the radiosonde/thermosonde combination and conducted the scintillometer measurements.

The plan was to operate all instruments simultaneously but this was not possible. Personnel, scheduling, and weather conflicts, to a great extent, dictated when each instrument was available. Consequently, experiments were conducted with two or three of the instruments: thermosondes and radar; radar and scintillometer; thermosondes, radar, and aircraft.

3. THEORY

3.1 Thermosonde

The AFGL thermosonde¹ is an ac wheatstone bridge that measures small resistance differences between two unheated tungsten wires exposed to the ambient atmosphere. A 2-m weather balloon carries the instrument to altitudes up to 30 km, and the downlink transmission is facilitated by a modified VIZ Corp. radiosonde. The probe wires are separated horizontally by 1 m and the difference in resistance is translated to a difference in temperature by laboratory calibration and measurements of the temperature coefficient of resistance α of the tungsten probes. Specifically, $R_p = R_o + \alpha R_o (T - T_o)$, where α is evaluated at temperature $T_o = 0^\circ \text{C}$. The inertial range refractive index structure parameter, C_n^2 is calculated² from the expression:

$$C_n^2(z) = \left[79.9 \times 10^{-6} \frac{P(z)}{T^2(z)} \right]^2 C_T^2(z)$$

where $P(z)$ is pressure in mbar and z is altitude. C_T^2 is the temperature structure parameter, and it is evaluated from the mean square temperature fluctuation as provided by the thermosonde. Pressure, temperature, humidity, and C_T are

2. Tatarski, V. I. (1961) Wave Propagation in a Turbulent Medium, McGraw-Hill Co., New York.

sampled by the radiosonde and transmitted once every 2 sec or about every 10 m altitude. Altitude could be obtained independently from the tracking data.

3.2 Radar

The Millstone Hill 440-MHz radar was operated by Northeast Radio Observatory Corporation personnel³ to measure continuous altitude profiles of C_n^2 . Fluctuations in the atmospheric index of refraction arising from gradients in temperature and humidity generated by turbulence were the source of signal returns from the sensitive UHF radar. Turbulence is evaluated from the wind shifted Doppler frequency spectrum of the signal.

The radar volume reflectivity η is related to C_n^2 by⁴

$$C_n^2 = (\eta / 0.33) \lambda^{1/3}$$

where λ is the radar wavelength. The scattering is assumed to arise from homogeneous isotropic turbulence that fills the entire scattering volume. The reflectivity is related to the measured signal to noise ratio, SNR, by⁵

$$\eta = R_c \frac{\Delta r}{r^2} (\text{SNR})$$

where R_c is the radar calibration constant, r is the radar slant range, and Δr is the range gate resolution. The radar azimuth and elevation angles were aligned as close as possible with the radiosonde path, but not so close as to cause interference. In these experiments, the radar had a height resolution of about 1 km with each profile being evaluated approximately every minute. Data below 5 km were eliminated so as to eliminate large ground clutter noise and to avoid high sensitivity to water vapor. Data above 18 km were not reliable due to the small SNR in this region.

3.3 Stellar Scintillometer

The stellar scintillometer is a 36-cm Schmidt-Cassegrain telescope that focuses starlight into an attached instrument assembly. The scintillation intensity is measured at three different spatial wavelengths between 5 and 15 cm. These spatial

3. Good, R. E., Watkins, B. J., Quesada, A. F., Brown, J. H., and Lorient, G. B. (1982) Radar and optical measurements of C_n^2 , Appl. Opt., 21:3373-3376.
4. Ottersten, H. H. (1969) Radar backscattering from the turbulent clear atmosphere, Radio Science, 4:1251-1255.
5. Balsley, B. B., and Gage, K. S. (1980) The MST radar technique potential for middle atmospheric studies, Pure Appl. Geophys., 118:452.

wavelengths are linearly combined to form seven composite path⁶ - weighting functions to provide seven different altitude regions of the turbulence measurements. Halfwidths of the weighting functions increase from 1.4 km at 2.25 km altitude to 6.0 km at 18 km altitude. C_n^2 is calculated from the normalized stellar irradiance variance detected through the spatial filter,

$$\sigma_{I_f}^2 \text{ where } \sigma_{I_f}^2 = \left\{ \left[\ln(\bar{I}_1 + I_1') - \ln(\bar{I}_2 + I_2') \right]^2 \right\}^{1/2}$$

and \bar{I}_1 and I_1' are the mean and fluctuating part of the signal passed by the filter reticle and \bar{I}_2 and I_2' are the mean and fluctuating part of the signal reflected by the filter reticle.

3.4 Aircraft Measurements

Airborne Research Associates (ARA), under contract to AFGL, equipped an aircraft with 4.5 μm diameter heated tungsten wires. These were mounted on a wingtip, one above the other with a separation of 0.85 m. Wheatstone bridge measurements of the voltage difference between the two wires were recorded along with simultaneous measurements⁷ of air temperature, pressure, humidity, and airspeed. C_T^2 was calculated from:

$$C_T^2 = \left\{ (\Delta T_{\text{rms}})^2 - N^2 \right\} d^{-2/3}$$

where N is the noise level with contributions from the bridge and from velocity fluctuations. The noise level was estimated by measuring the bridge voltage under relatively quiet signal conditions. Additionally, the contribution due to velocity fluctuations was sensed by a single hot wire and a constant temperature anemometer bridge. C_n^2 was then calculated from C_T^2 in the same manner as for the thermosonde.

4. RAWINSONDE RESULTS

4.1 Temperature and Humidity

Ambient temperature was measured by a thermistor rod mounted on a plastic outrigger attached to the radiosonde. Relative humidity was measured by a carbon

6. Ochs, G.R., Wang, T., Lawrence, R.S., Clifford, S.F. (1976) Refractive-turbulence profiles measured by one-dimensional spatial filtering of scintillations, Appl. Opt., 15:2564-2510.

7. Fairall, C.W., and Markson, R. (1979) Aircraft Measurements of Micro-Meteorological Parameters at Panama City, Florida in 1978, Naval Postgraduate School Technical report.

hygristor mounted in a flow duct inside the radiosonde. These measurements were sampled every 2 sec or about every 10 m. Figures 1-19 are profiles of temperature and relative humidity for 19 flights. Since the hygristor is insensitive to relative humidity below 20 percent, the relative humidity plots are cut off at 10 km where this condition normally prevails.

4.2 Wind Speed and Direction

A technique based upon radio signal phase shift was used to measure the balloon's position as a function of time. Derivatives of the position are evaluated to estimate wind speed and direction. Figures 20-36 are profiles of the wind speed and direction of 17 flights. Outlier points were removed and the raw data smoothed and filtered by a low pass filter whose cutoff was about 0.03 Hz.

Mean square wind speeds, $\overline{W^2}$, are evaluated for these flights for use in the Hufnagel⁸ C_n^2 model. Values of $\overline{W^2}$ are listed in Table 1.

4.3 Thermosonde C_n^2 Profiles - Hufnagel Comparisons

Weighted 500-m log-averaged of the 10 m samples of thermosonde C_n^2 data are plotted in Figures 37-50. The weighted average is calculated from

$$C_n^2(z) = \frac{n}{N} \log^{-1} \left\{ \frac{1}{N} \sum_{i=1}^n \log C_{n_i}^2 \right\}$$

where N is the total number of points over $\Delta z = 500$ m, and n is the number of points above the thermosonde noise limit of 0.002°C . The noise limit is reached in regions of very low turbulence. A logarithmic average is performed since C_n^2 is represented by a log-normal distribution. The mean, multiplied by or divided by one standard deviation, is shown on either side of the mean. The curves are broken and replaced by circles where radio loss of signal occurs and/or where the number of data points, n, were small. Actual instantaneous C_n^2 data are plotted for the first 500 m above the surface since in this boundary layer region, C_n^2 falls off rapidly with altitude and a 500 m average is not representative. Obviously, the profiles are space- and time-dependent; however, the trend curve is considered valid over the length of the experiment.

To estimate the C_n^2 profile from rawinsonde meteorological data, Hufnagel⁸ developed a mean square wind speed dependent model. This simple empirical model depends only on $\overline{W^2}$, the mean square wind speed over 5 km to 20 km. For altitudes of 3 km to 24 km the model is given as,

8. Hufnagel, R. E. (1974) Variations of atmospheric turbulence, The Infrared Handbook, USGPO, Washington, D.C., Chapter 6, pp 1-56.

$$C_n^2(\text{Huf}) = 2.7 \times 10^{-16} \left\{ 3 \overline{W^2} e^{-z} \left(\frac{z}{10} \right)^{10} + e^{-\left(\frac{z}{1.5} \right)} \right\}.$$

Values of $\overline{W^2}$ are listed in Table 1. In three cases, QX45, QX35, and QX43, wind data are not obtained up to 20 km; nevertheless, $\overline{W^2}$ calculated to the maximum altitude is presented for comparison. Profiles calculated with the Hufnagel model are depicted in Figures 37-50 as solid dark lines. In most cases, order-of-magnitude agreement is found between the thermosonde C_n^2 profiles and the model. The trends are similar but, of course, the model as given above does not show turbulent layering structure, and it cannot be expected to match actual turbulence, which depends on the Richardson number and not on the wind speed alone. Further studies are being performed to compare the thermosonde data with a Van Zandt⁹ model, which does depend on Richardson number.

4.4 Averaged Thermosonde C_n^2 Profile

The C_n^2 data for the 10 day and 9 night flights results in the 500 m log-average profile shown in Figures 51 and 52. A comparison of the two profiles clearly shows a larger C_n^2 in the daytime, as seen in Figure 53. Starting near 5 km, the difference increases to a maximum value near 20 km where the difference is four times the nighttime C_n^2 . Above 20 km, the difference decreases, finally ending above 34 km altitude. A careful analysis of the microthermal probes (see Appendix A) indicates the diurnal difference cannot be attributed to solar heating of the probes.

An exponential quadratic model may be used to fit the average data. The model takes the form:

$$\log C_n^2 = A + Bz + Cz^2.$$

For $Z \geq 3.5$ km, the fitted constants are:

	10-Day-flights Averaged	9-Night-flights Averaged
A	-17.279	-16.953
B	+ 0.0852	- 0.0251
C	- 0.0045	- 0.0016

9. Van Zandt, T.E., Gage, K.S., and Warnock, J.M. (1981) An Improved Model for the Calculation of Profiles of C_n^2 and ϵ in the Free Atmosphere From Background Profiles of Wind, Temperature and Humidity, 20th Conference Radar Meteor. Soc., Boston, Amer. Met. Soc., pp 129-135.

For summer daytime conditions at the experiment coordinates, the model suggests dropoff rates (dB/km) = $10 \frac{d}{dz} \log(C_n^2)$ of -0.5 dB/km and -1.3 dB/km at 5 km and 30 km respectively. Nighttime conditions give -0.4 dB/km and -1.2 dB/km at 5 km and 30 km respectively. The daytime C_n^2 values are higher than the night values and it is assumed the faster daytime decrease of C_n^2 with altitude would continue until the day and night values coincide. Thereafter, they would both decrease at the night rate. If it is assumed that C_T^2 is constant with altitude, then the dB/km decrease can be interpreted as an atmospheric scale height (H) using the relationship

$$H = \frac{8.69}{(\text{dB/km})}.$$

The observed -1.2 dB/km at 30 km during the night is nearly identical to the standard atmosphere pressure scale height of 6.7 km (-1.29 dB/km).

4.5 Coherence Scales

For those flights where thermosonde C_n^2 exists, the transverse coherence length¹⁰ r_o and isoplanatic angle θ_o were calculated. The coherence length is

$$r_o = 1.6 \left\{ k^2 \int_{z_o}^{z_f} C_n^2(z) dz \right\}^{-3/5} \text{ (m)},$$

and the isoplanatic angle is

$$\theta_o = 0.52 \left\{ k^2 \int_{z_o}^{z_f} C_n^2(z) dz \right\}^{-3/5} \text{ (rad)},$$

where the wave number k is $2\pi/\lambda$, z_o is the observer altitude and z_f is the maximum altitude. Results of these calculations are shown in Table 1. Measurements of C_n^2 at 8-12 m intervals were logarithmically interpolated to 10 m intervals and data in the noise were set to C_T (noise) = 0.002.

For those flights having data at least to 16 km, the total log-average of the isoplanatic angle θ_o is calculated for day and night conditions. The coherence length r_o could be calculated including the two low altitude flights. The averaged values are,

$$\begin{aligned} \overline{r_o} &= 6.7 \pm 1.2 \text{ cm} && \text{Day} \\ \overline{\theta_o} &= 2.4 \pm 0.5 \mu\text{rad} \\ \overline{r_o} &= 7.6 \pm 2.4 \text{ cm} && \text{Night} \\ \overline{\theta_o} &= 5.1 \pm 1.1 \mu\text{rad} \end{aligned}$$

where the errors are ± 1 standard deviation. As expected,¹¹ daytime conditions provide smaller values of the coherence length and thus harsher conditions with which a particular optical system must contend.

10. Fried, D.L. (1966) Optical resolution through a randomly inhomogeneous medium for very long and very short exposures, J. Opt. Soc. Am., 56:1372-1379.

11. Walters, D.L., Favier, D.L., and Hines, J.R. (1979) Vertical path measurements MTF measurements, J. Opt. Soc. Am., 69:828-837.

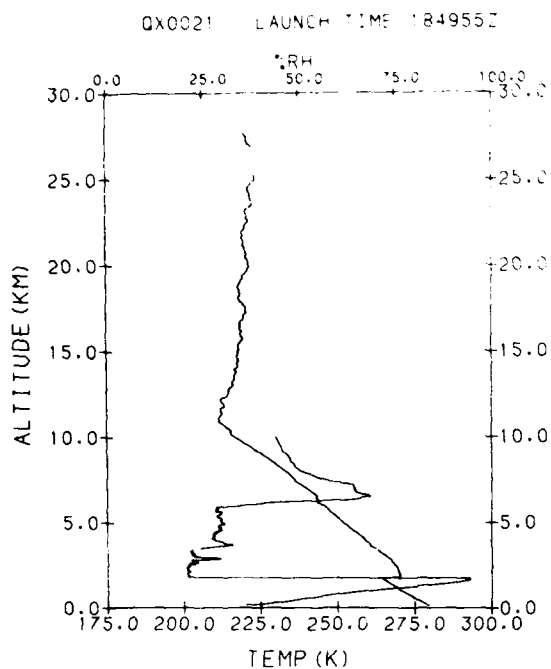


Figure 1. Radiosonde Ambient Temperature and Relative Humidity Profiles - Flight QX0021. Launched at 1850Z on 23 Mar 1983. Humidity data are truncated above approximately 10 km

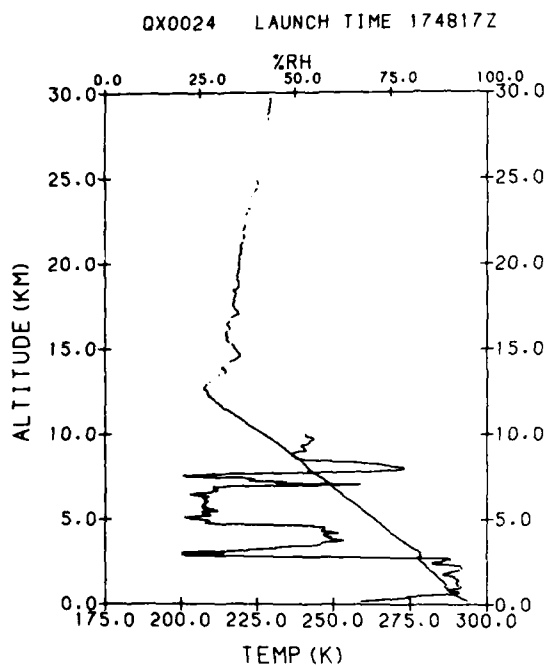


Figure 2. Radiosonde Ambient Temperature and Relative Humidity Profiles - Flight QX0024. Launched at 1749Z on 15 May 1983. Humidity data are truncated above approximately 10 km

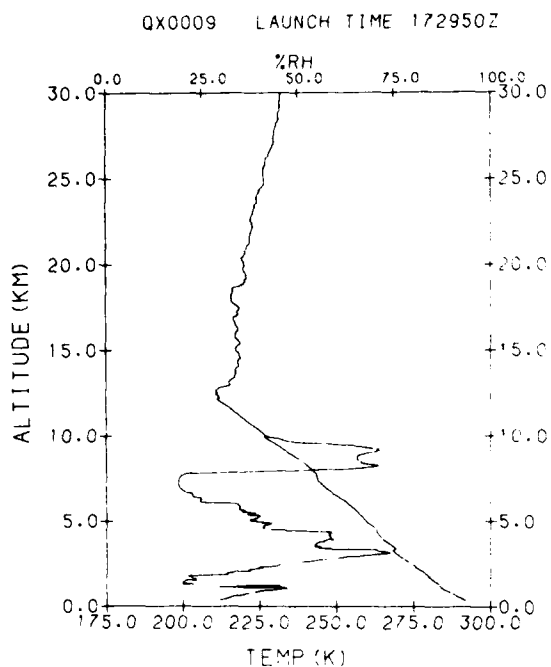


Figure 3. Radiosonde Ambient Temperature and Relative Humidity Profiles - Flight QX0009. Launched at 1730Z on 21 May 1983. Humidity data are truncated above approximately 10 km

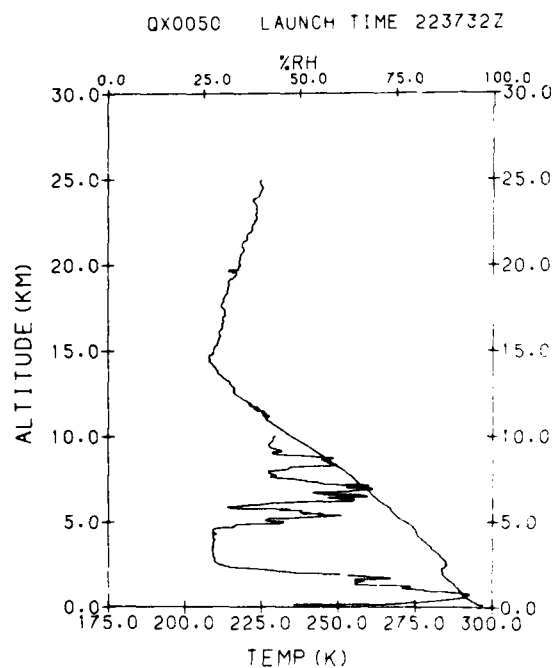


Figure 4. Radiosonde Ambient Temperature and Relative Humidity Profiles - Flight QX0050. Launched at 2238Z on 30 June 1983. Humidity data are truncated above approximately 10 km

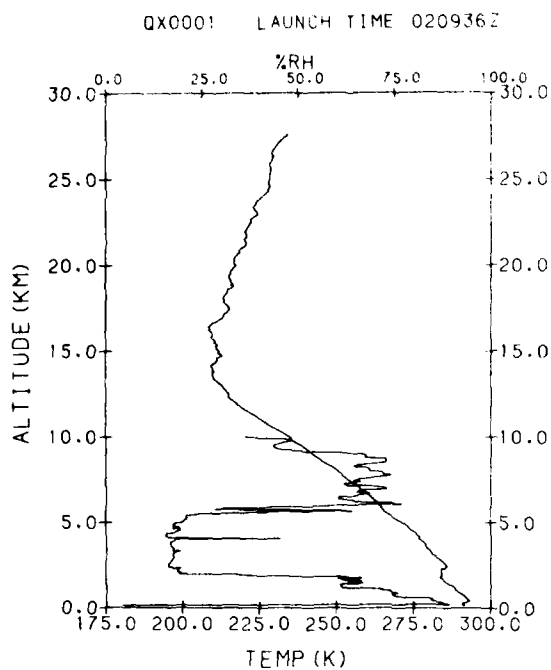


Figure 5. Radiosonde Ambient Temperature and Relative Humidity Profiles - Flight QX0001. Launched at 0210Z on 1 July 1983. Humidity data are truncated above approximately 10 km

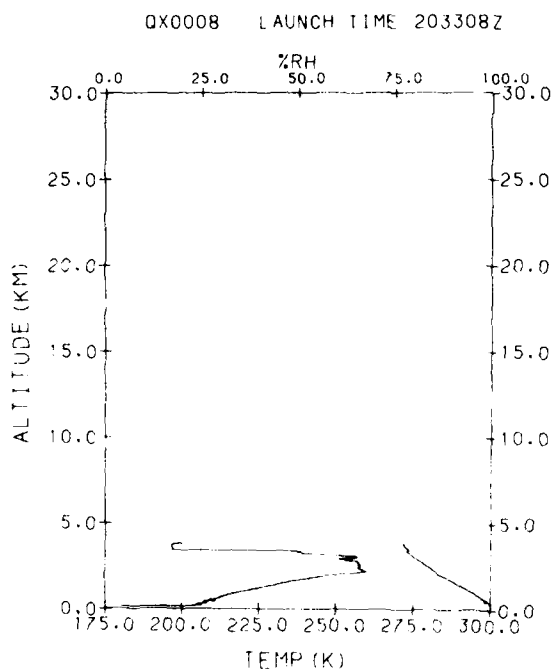


Figure 6. Radiosonde Ambient Temperature and Relative Humidity Profiles - Flight QX0008. Launched at 2033Z on 11 July 1983. Humidity data are truncated above approximately 10 km

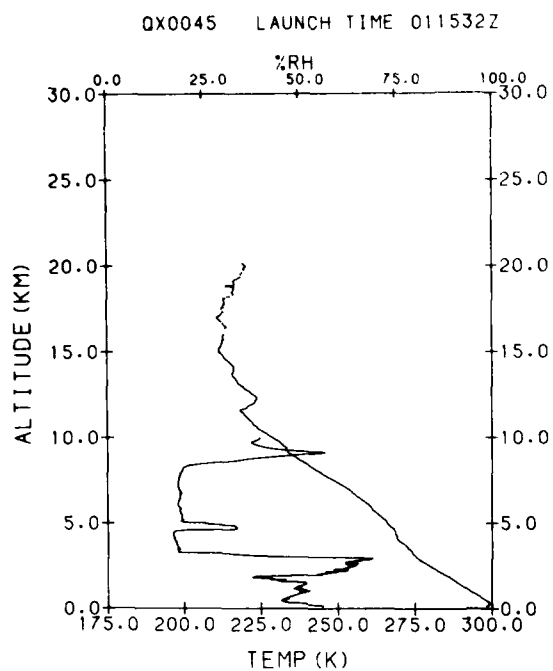


Figure 7. Radiosonde Ambient Temperature and Relative Humidity Profiles - Flight QX0045. Launched at 0116Z on 12 July 1983. Humidity data are truncated above approximately 10 km

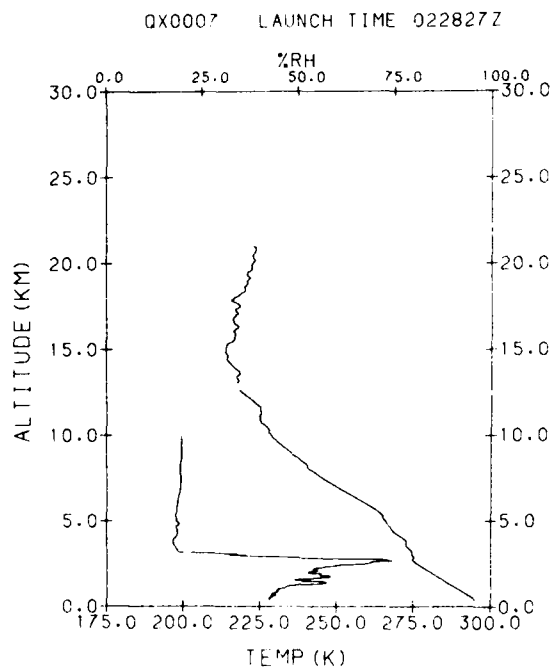


Figure 8. Radiosonde Ambient Temperature and Relative Humidity Profiles - Flight QX0007. Launched at 0228Z on 16 July 1983. Humidity data are truncated above approximately 10 km

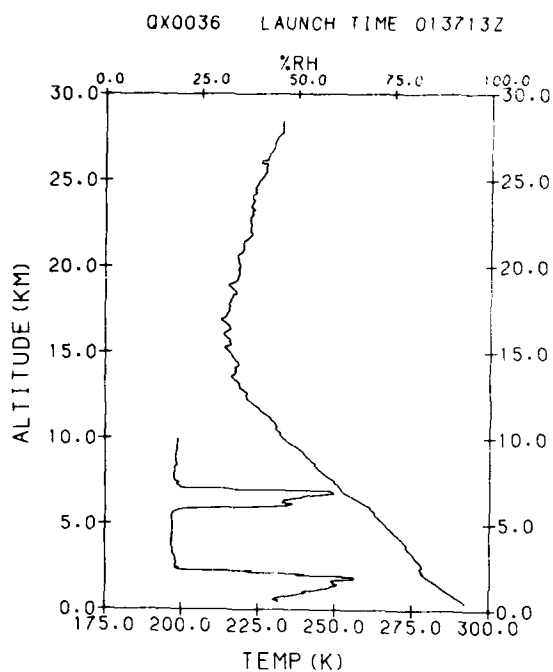


Figure 9. Radiosonde Ambient Temperature and Relative Humidity Profiles - Flight QX0036. Launched at 0137Z on 23 July 1983. Humidity data are truncated above approximately 10 km

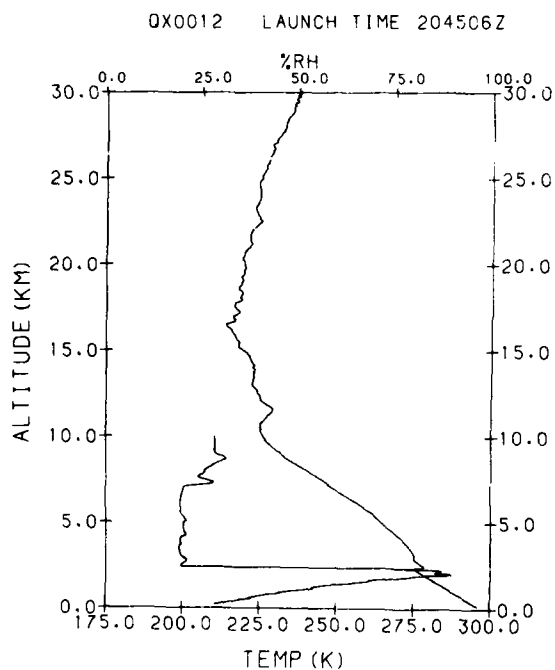


Figure 10. Radiosonde Ambient Temperature and Relative Humidity Profiles - Flight QX0012. Launched at 2045Z on 23 July 1983. Humidity data are truncated above approximately 10 km

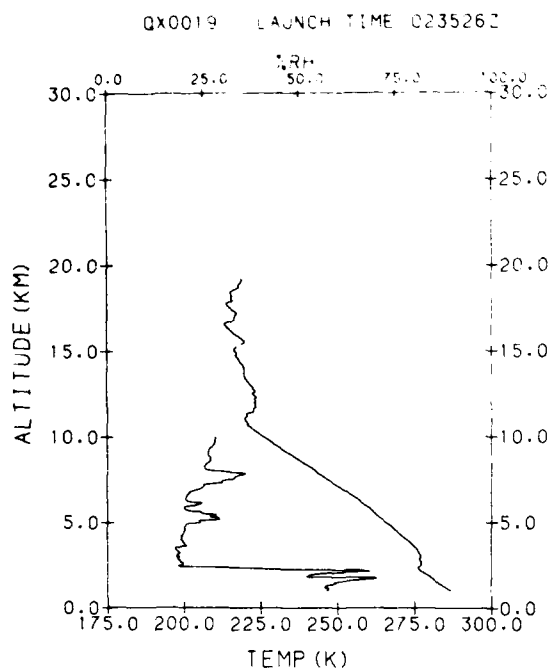


Figure 11. Radiosonde Ambient Temperature and Relative Humidity Profiles - Flight QX0019. Launched at 0235Z on 24 July 1983. Humidity data are truncated above approximately 10 km

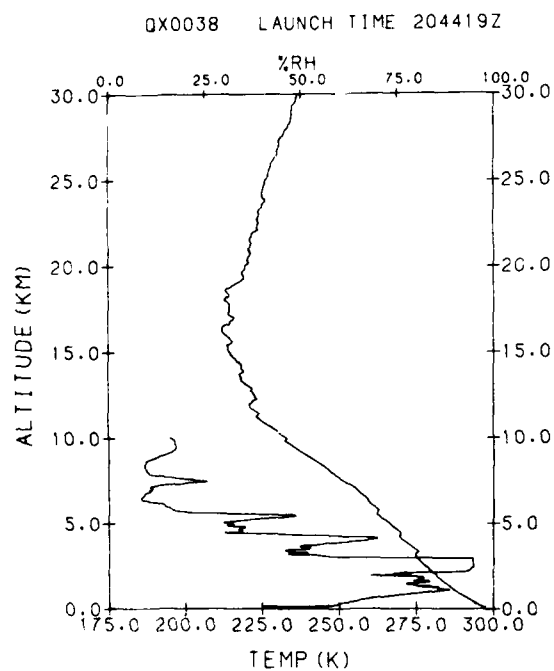


Figure 12. Radiosonde Ambient Temperature and Relative Humidity Profiles - Flight QX0038. Launched at 2044Z on 25 July 1983. Humidity data are truncated above approximately 10 km

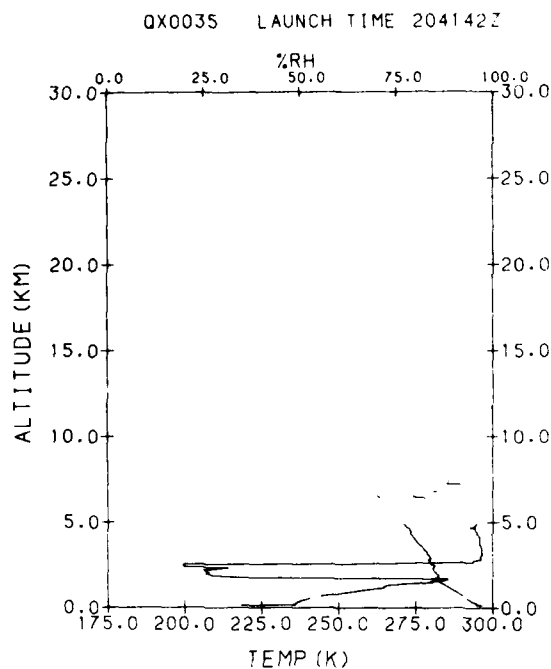


Figure 13. Radiosonde Ambient Temperature and Relative Humidity Profiles - Flight QX0035. Launched at 2042Z on 28 July 1983. Humidity data are truncated above approximately 10 km

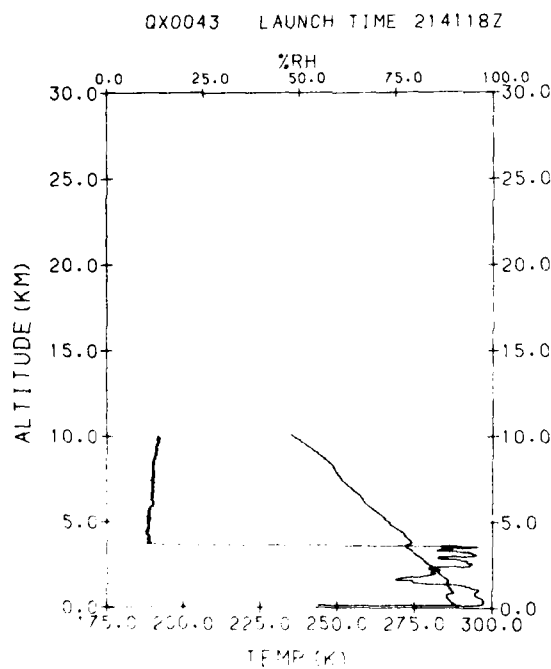


Figure 14. Radiosonde Ambient Temperature and Relative Humidity Profiles - Flight QX0043. Launched at 2141Z on 29 July 1983. Humidity data are truncated above approximately 10 km

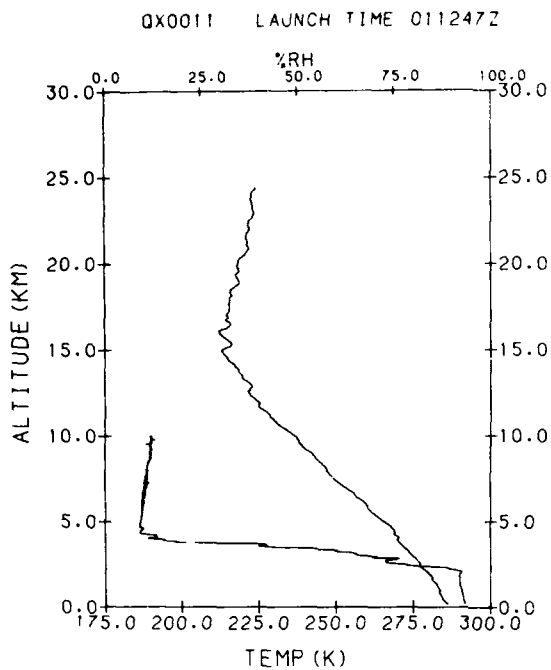


Figure 15. Radiosonde Ambient Temperature and Relative Humidity Profiles - Flight QX0011. Launched at 0113Z on 30 July 1983. Humidity data are truncated above approximately 10 km

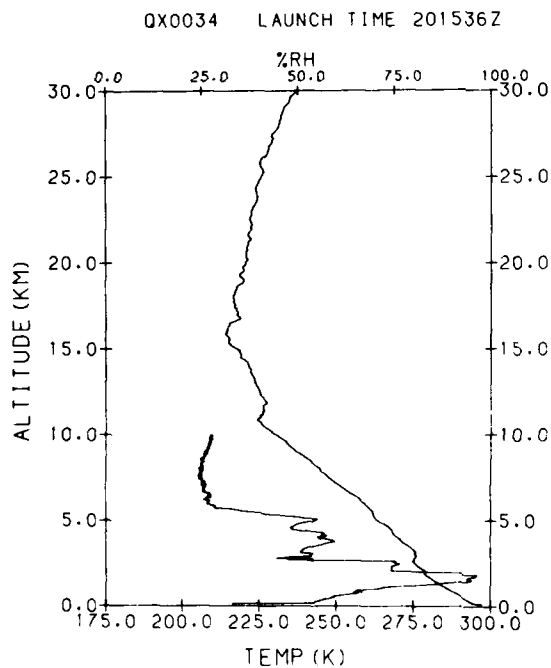


Figure 16. Radiosonde Ambient Temperature and Relative Humidity Profiles - Flight QX0034. Launched at 2016Z on 30 July 1983. Humidity data are truncated above approximately 10 km

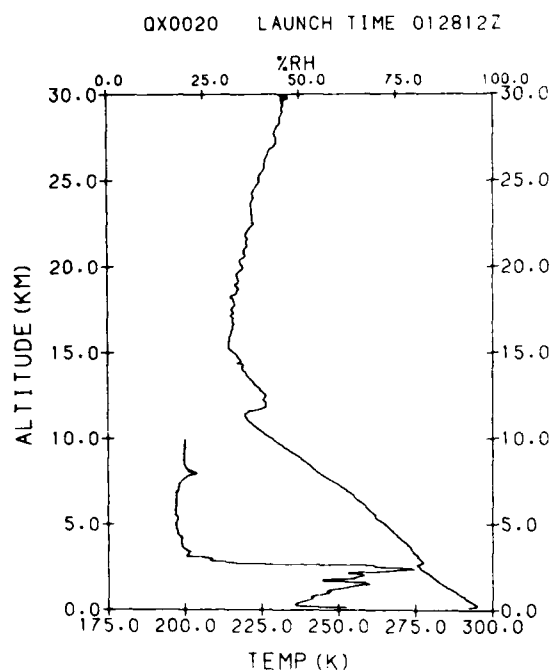


Figure 17. Radiosonde Ambient Temperature and Relative Humidity Profile - Flight QX0020. Launched at 0128Z on 31 July 1983. Humidity data are truncated above approximately 10 km

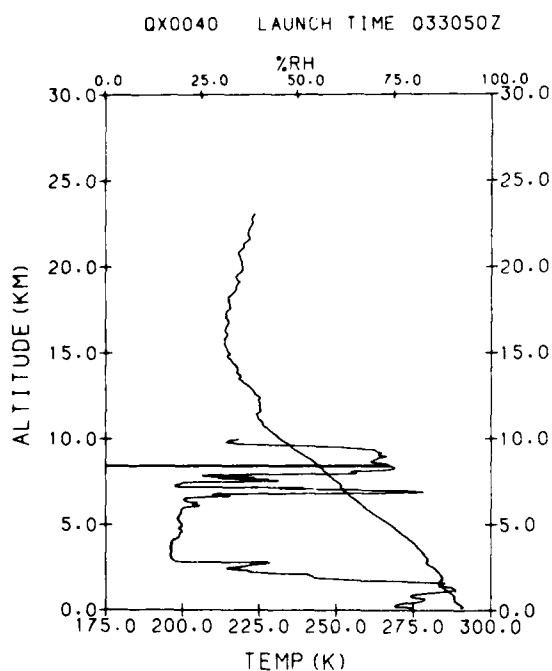


Figure 18. Radiosonde Ambient Temperature and Relative Humidity Profiles - Flight QX0040. Launched at 0331Z on 7 Aug 1983. Humidity data are truncated above approximately 10 km

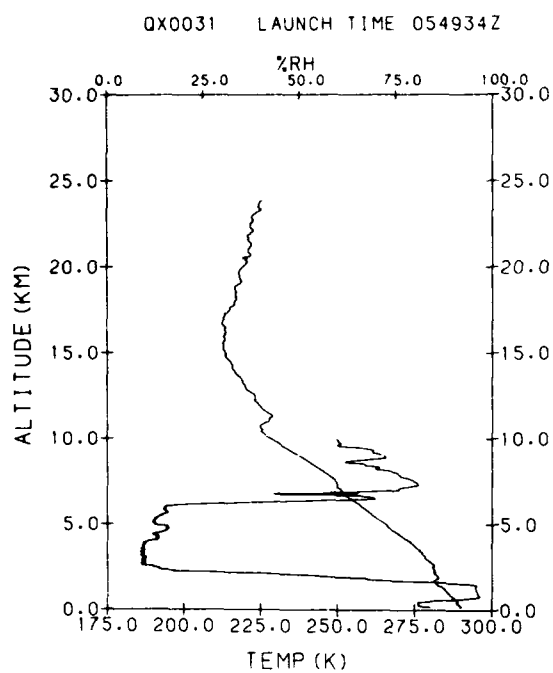


Figure 19. Radiosonde Ambient Temperature and Relative Humidity Profiles - Flight QX0031. Launched at 0550Z on 8 Aug 1983. Humidity data are truncated above approximately 10 km

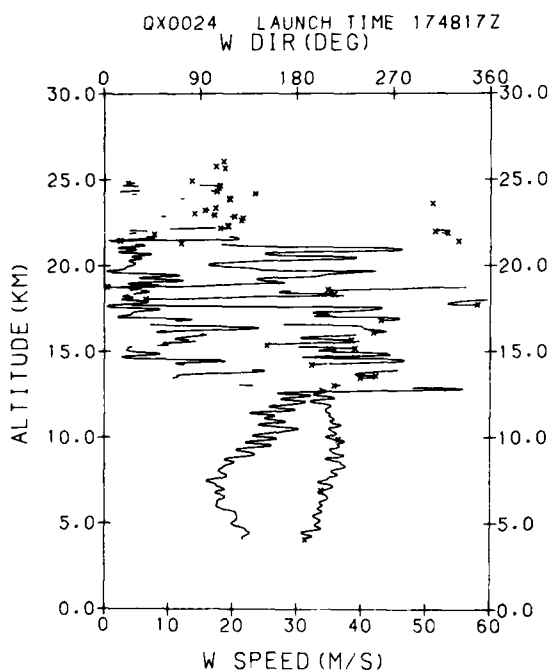


Figure 20. Winds Aloft Profile - Flight QX0024. Launched at 1749Z on 15 May 1983

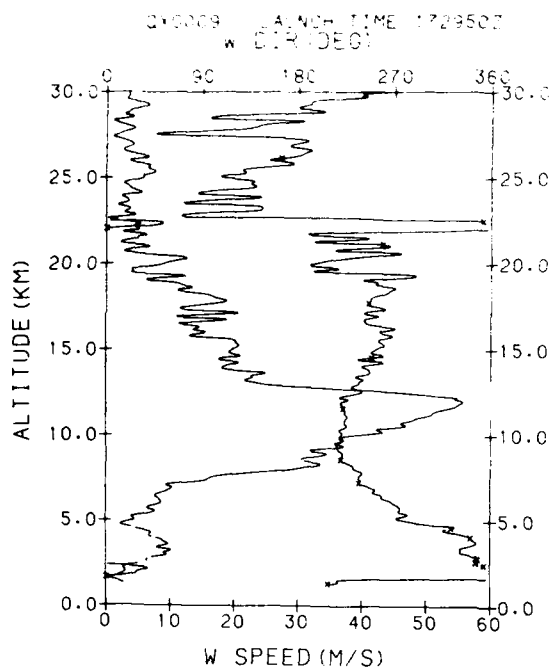


Figure 21. Winds Aloft
Profile - Flight QX0009.
Launched at 1730Z on
21 May 1983

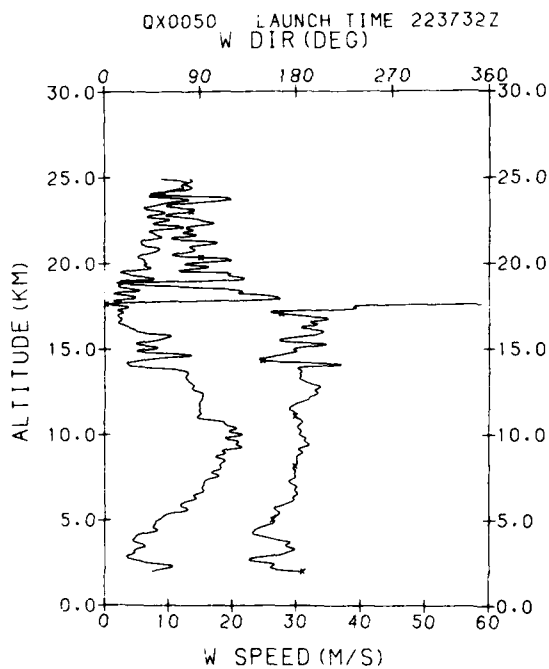


Figure 22. Winds Aloft
Profile - Flight QX0050.
Launched at 2238Z on
30 June 1983

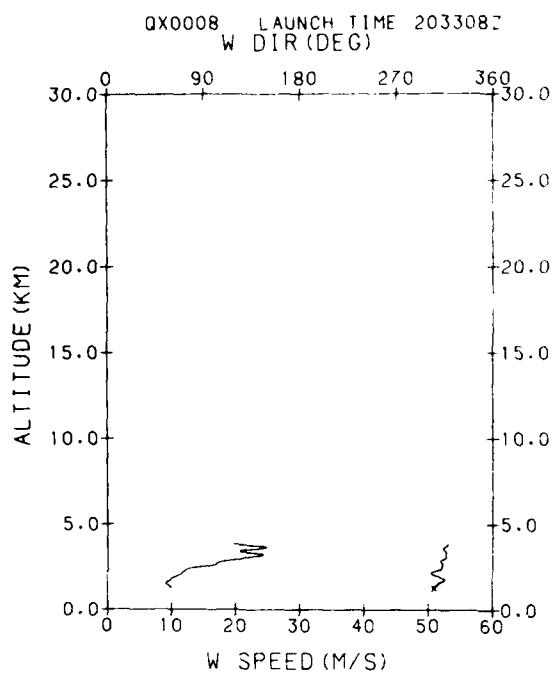


Figure 23. Winds Aloft
Profile - Flight QX0008.
Launched at 2033Z on
11 July 1983

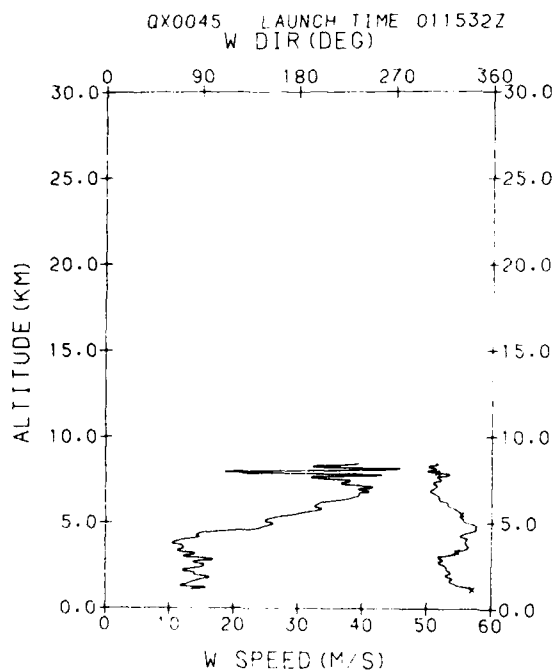


Figure 24. Winds Aloft
Profile - Flight QX0045.
Launched at 0116Z on
12 July 1982

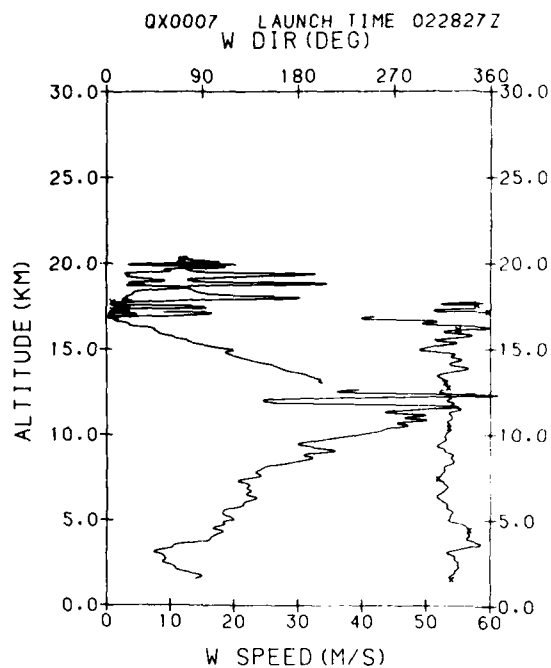


Figure 25. Winds Aloft
Profile - Flight QX0007.
Launched at 0228Z on
16 July 1983

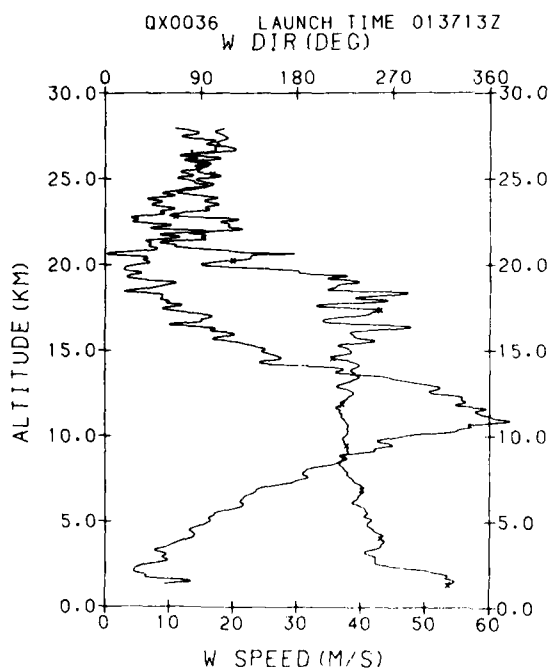


Figure 26. Winds Aloft
Profile - Flight QX0036.
Launched at 0137Z on
23 July 1983

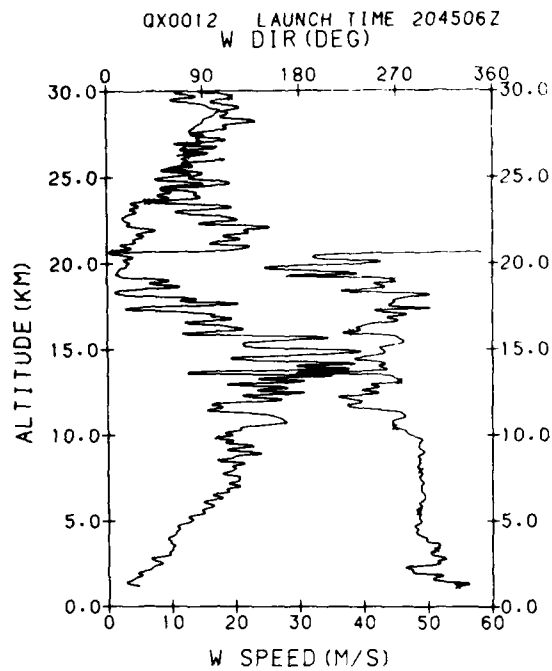


Figure 27. Winds Aloft
Profile - Flight QX0012.
Launched at 2045Z on
23 July 1983

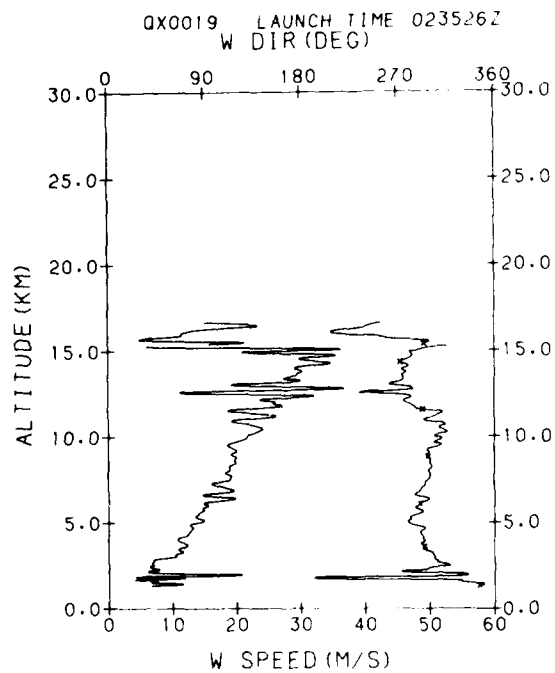


Figure 28. Winds Aloft
Profile - Flight QX0019.
Launched at 0235Z on
24 July 1983

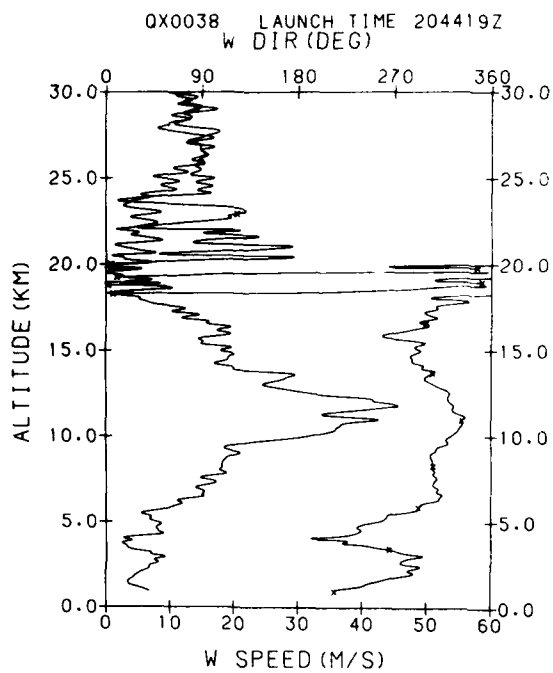


Figure 29. Winds Aloft
Profile - Flight QX0038.
Launched at 2044Z on
25 July 1983

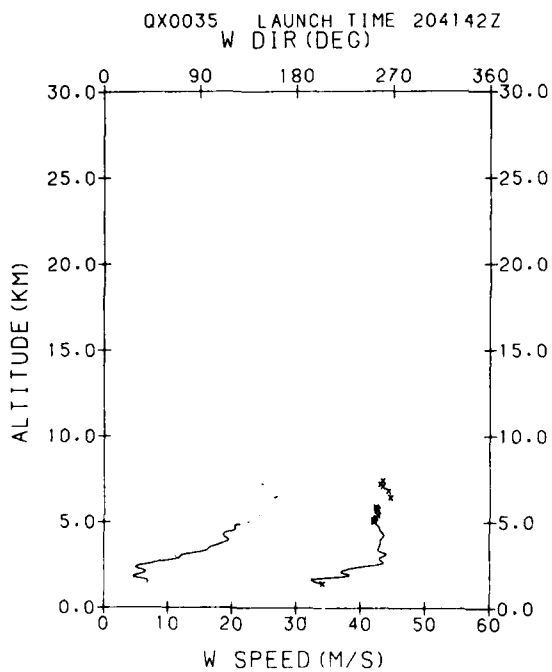


Figure 30. Winds Aloft
Profile - Flight QX0035.
Launched at 2042Z on
28 July 1983

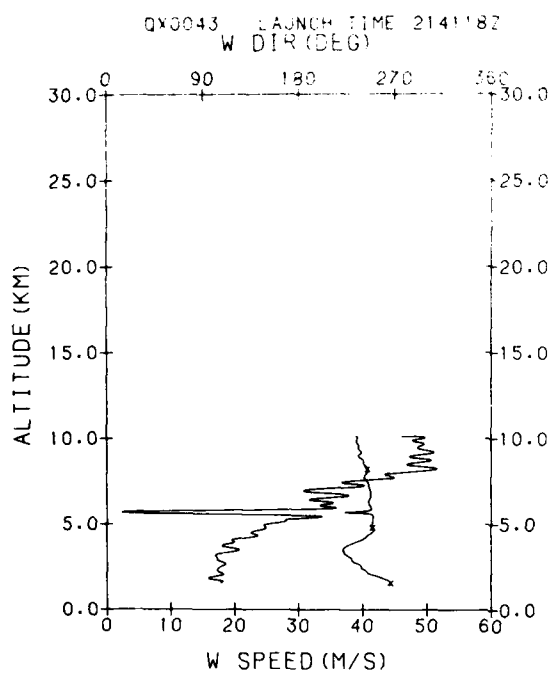


Figure 31. Winds Aloft
Profile - Flight QX0043.
Launched at 2141Z on
29 July 1983

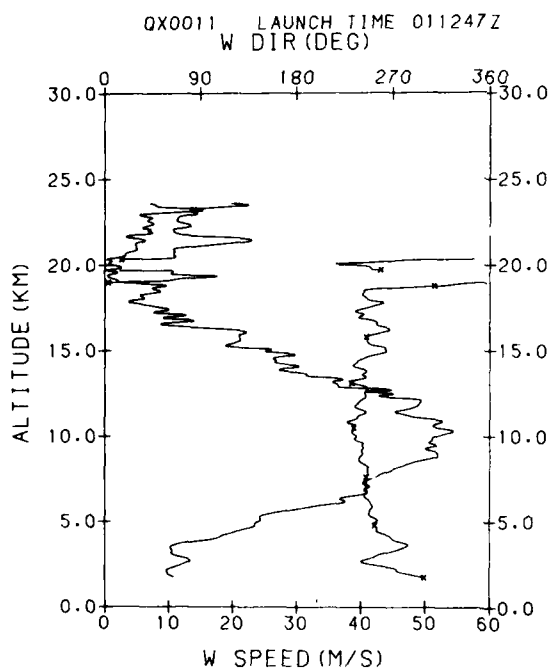


Figure 32. Winds Aloft
Profile - Flight QX0011.
Launched at 0113Z on
30 July 1983

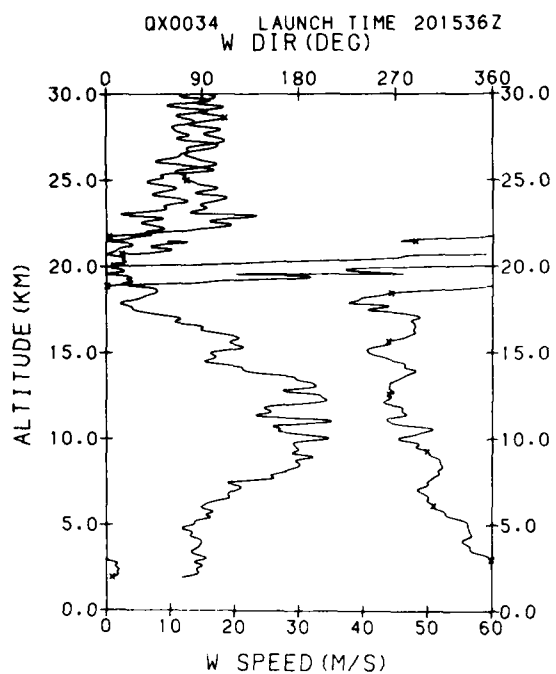


Figure 33. Winds Aloft
Profile - Flight QX0034.
Launched at 2016Z on
30 July 1983

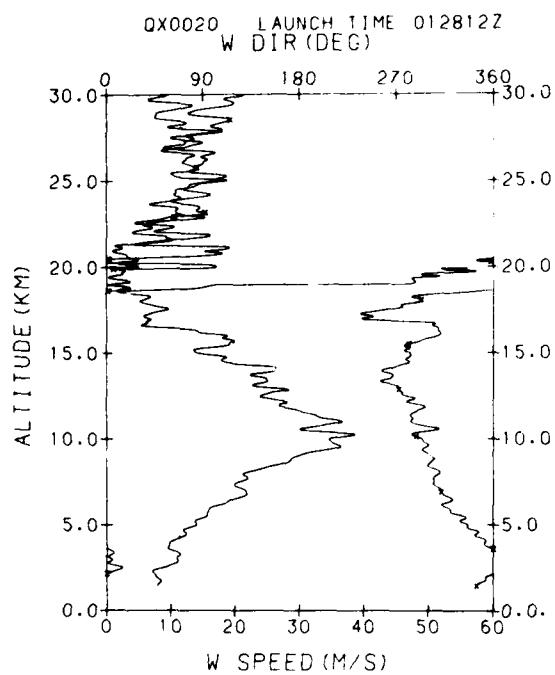


Figure 34. Winds Aloft
Profile - Flight QX0020.
Launched at 0128Z on
31 July 1983

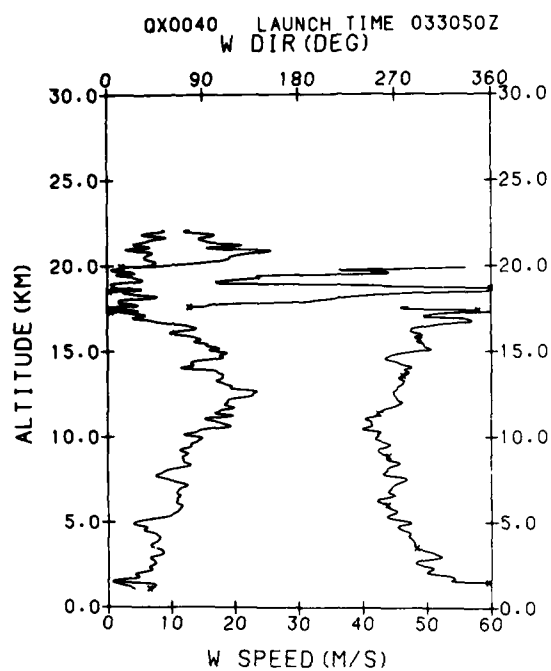


Figure 35. Winds Aloft
Profile - Flight QX0040.
Launched at 0331Z on
7 Aug 1983

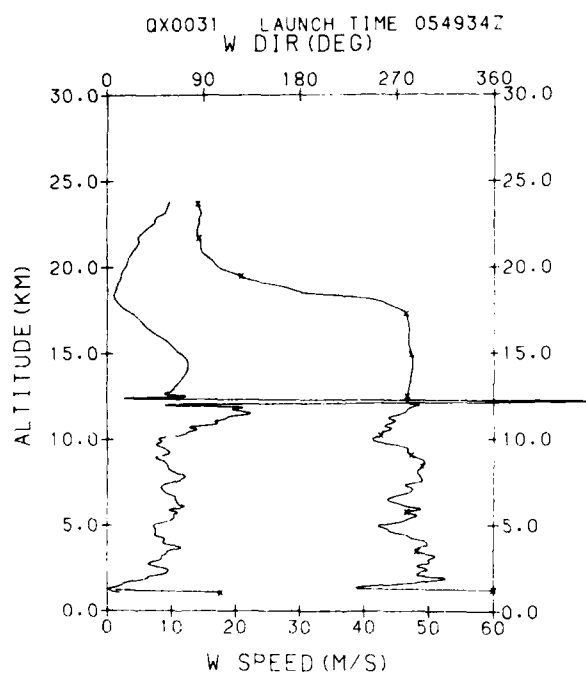


Figure 36. Winds Aloft
Profile - Flight QX0031.
Launched at 0550Z on
8 Aug 1983

Table 1. Balloon Flight Parameters

Launch Date	(UT) Time	Flight ID	$\overline{W^2}$ (m ² sec ⁻²)	r_o (cm)	θ_o (μ rad)	Max. Alt. (km)	Max. Wind Alt (km)	Day/ Night
23 Mar	1850	QX21	-	6.7	2.6	27.6	-	D
15 May	1800	QX24	389.	5.6	2.2	29.6	26.6	D
21 May	1730	QX09	-	-	-	32.9	32.4	D
30 Jun	2237	QX50	163.	8.2	3.1	24.9	25.8	D
1 Jul	0210	QX01	-	-	-	27.6	-	N
11 Jul	2033	QX08	-	-	-	3.4	4.0	D
12 Jul	0116	QX45	1250.	5.4	3.2	19.5	8.0	N
16 Jul	0229	QX07	-	-	-	21.0	22.6	N
23 Jul	0137	QX36	1249.	10.3	6.7	28.4	28.7	N
23 Jul	2045	QX12	415.	7.6	2.6	31.9	32.5	D
24 Jul	0236	QX19	-	-	-	19.1	16.5	N
25 Jul	2044	QX38	484.	5.4	2.1	34.5	33.1	D
28 Jul	2042	QX35	619.*	7.4	-	7.4	7.3	D
29 Jul	2141	QX43	1805.*	7.5	-	10.1	10.3	D
30 Jul	0113	QX11	1256.	7.8	3.8	24.4	23.9	N
30 Jul	2016	QX34	472.	5.0	1.6	30.0	31.1	D
31 Jul	0128	QX20	469.	10.7	5.7	31.0	31.0	N
7 Aug	0331	QX40	179.	5.5	4.5	22.9	22.2	N
8 Aug	0549	QX31	158.	6.1	4.7	23.8	25.8	N

$\overline{W^2}$ \equiv mean square wind speed from 5 to 20 km (or maximum altitude)

r_o \equiv coherence length

θ_o \equiv isoplanatic angle

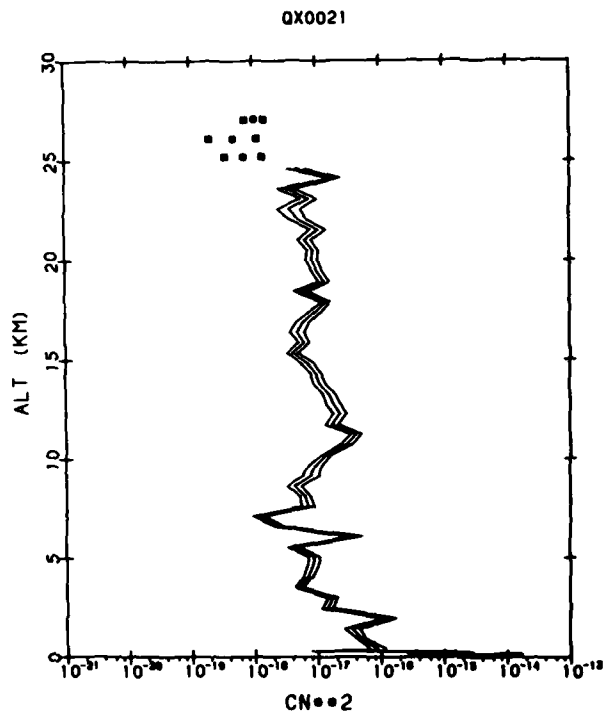


Figure 37. Log-Average C_n^2 Thermosonde Profiles and the Hufnagel Model - Flight QX0021. Launched at 1850Z on 23 Mar 1983. Thermosonde values were averaged every 500 m, and curves showing the mean multiplied by, and divided by, 1 sigma values are shown on either side of the mean

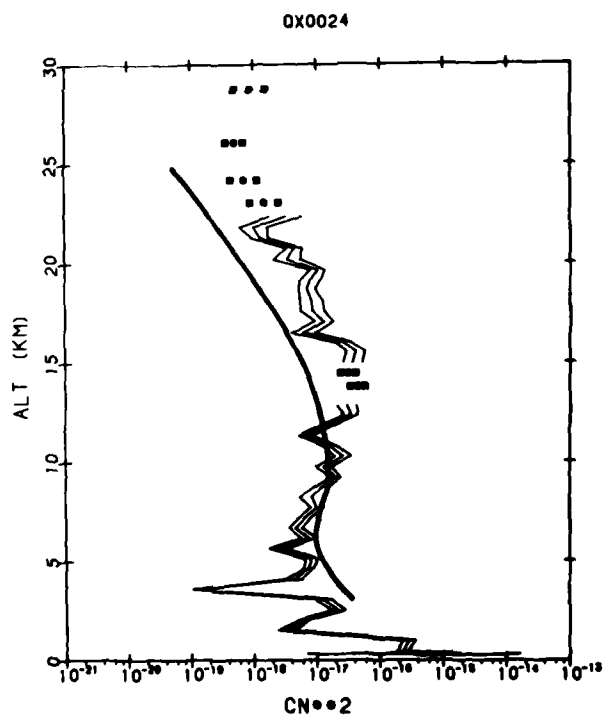


Figure 38. Log-Average C_n^2 Thermosonde Profiles and the Hufnagel Model - Flight QX0024. Launched at 1749Z on 15 May 1983. Thermosonde values were averaged every 500 m, and curves showing the mean multiplied by, and divided by, 1 sigma values are shown on either side of the mean. The thick line shows the C_n^2 values from the Hufnagel model

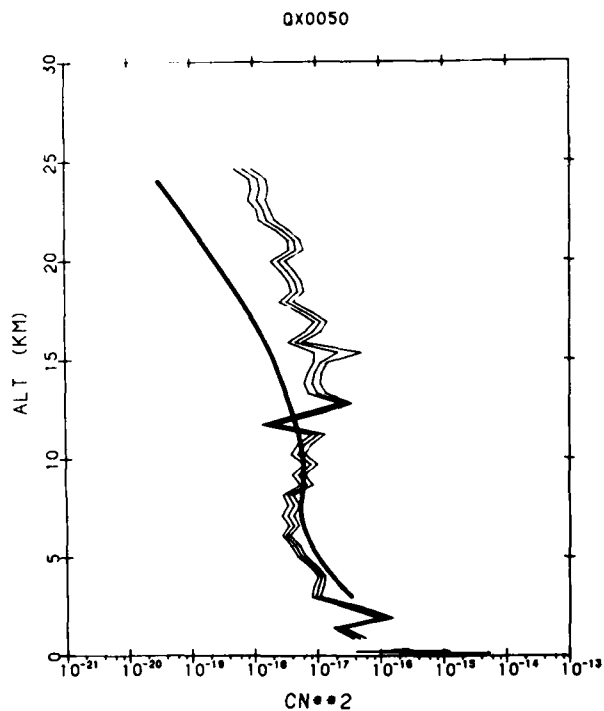


Figure 39. Log-Average C_n^2 Thermosonde Profiles and the Hufnagel Model - Flight QX0050. Launched at 2238Z on 30 June 1983. Thermosonde values were averaged every 500 m, and curves showing the mean multiplied by, and divided by, 1 sigma values are shown on either side of the mean. The thick line shows the C_n^2 values from the Hufnagel model

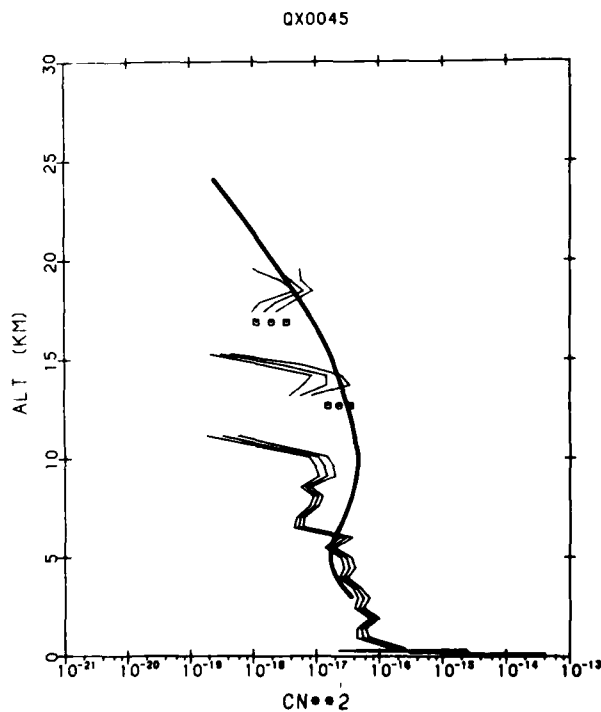


Figure 40. Log-Average C_n^2 Thermosonde Profiles and the Hufnagel Model - Flight QX0045. Launched at 0116Z on 12 July 1983. Thermosonde values were averaged every 500 m, and curves showing the mean multiplied by, and divided by, 1 sigma values are shown on either side of the mean. The thick line shows the C_n^2 values from the Hufnagel model

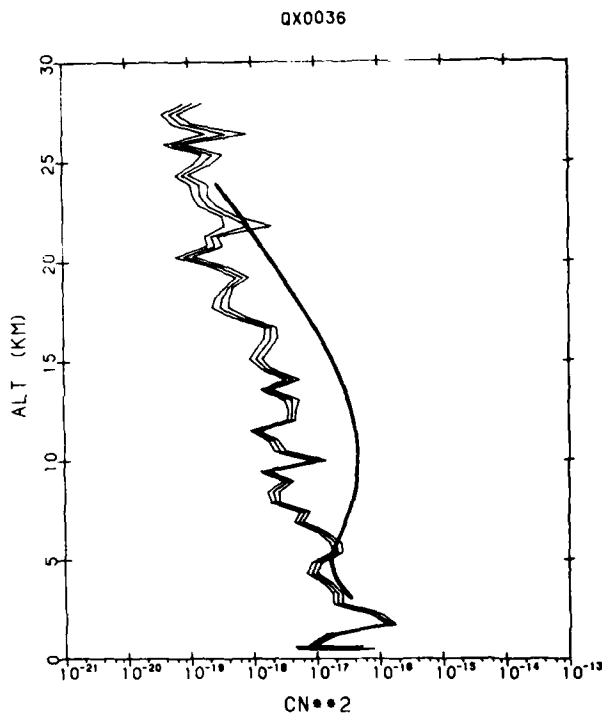


Figure 41. Log-Average C_n^2 Thermosonde Profiles and the Hufnagel Model - Flight QX0036. Launched at 0137Z on 23 July 1983. Thermosonde values were averaged every 500 m, and curves showing the mean multiplied by, and divided by, 1 sigma values are shown on either side of the mean. The thick line shows the C_n^2 values from the Hufnagel model

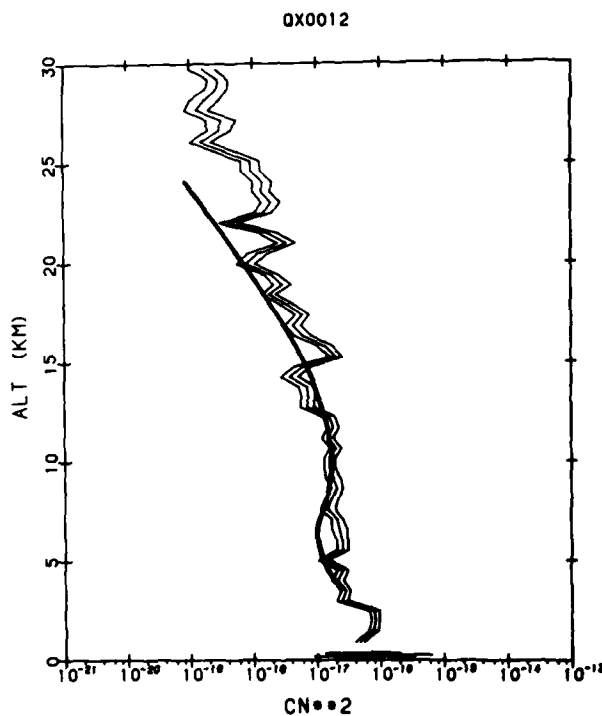


Figure 42. Log-Average C_n^2 Thermosonde Profiles and the Hufnagel Model - Flight QX0012. Launched at 2045Z on 23 July 1983. Thermosonde values were averaged every 500 m, and curves showing the mean multiplied by, and divided by, 1 sigma values are shown on either side of the mean. The thick line shows the C_n^2 values from the Hufnagel model

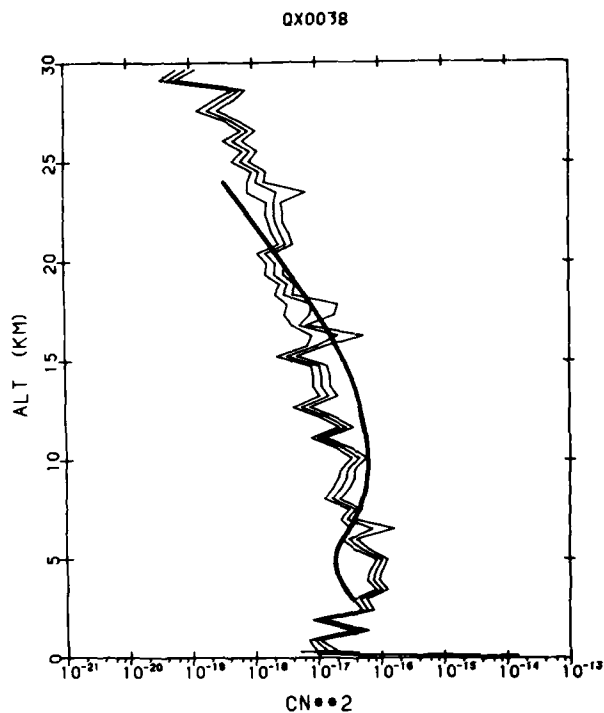


Figure 43. Log-Average C_n^2 Thermosonde Profiles and the Hufnagel Model - Flight QX0038. Launched at 2044Z on 25 July 1983. Thermosonde values were averaged every 500 m, and curves showing the mean multiplied by, and divided by, 1 sigma values are shown on either side of the mean. The thick line shows the C_n^2 values from the Hufnagel model

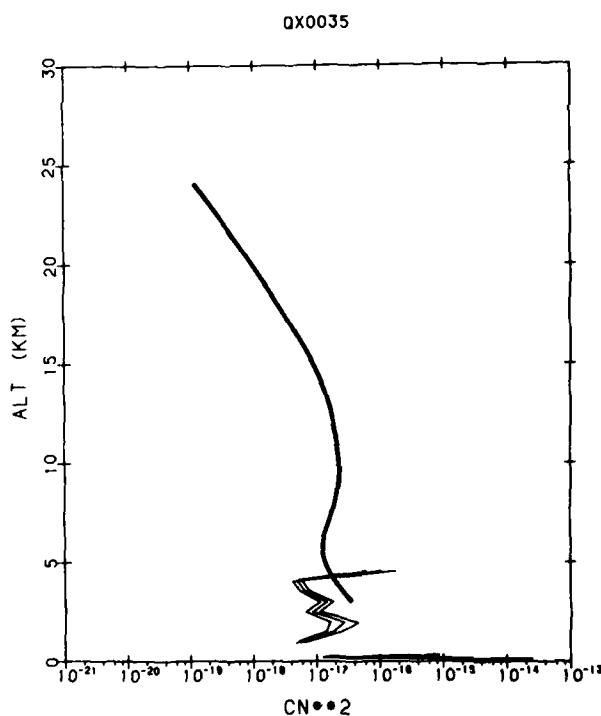


Figure 44. Log-Average C_n^2 Thermosonde Profiles and the Hufnagel Model - Flight QX0035. Launched at 2042Z on 28 July 1983. Thermosonde values were averaged every 500 m, and curves showing the mean multiplied by, and divided by, 1 sigma values are shown on either side of the mean. The thick line shows the C_n^2 values from the Hufnagel model

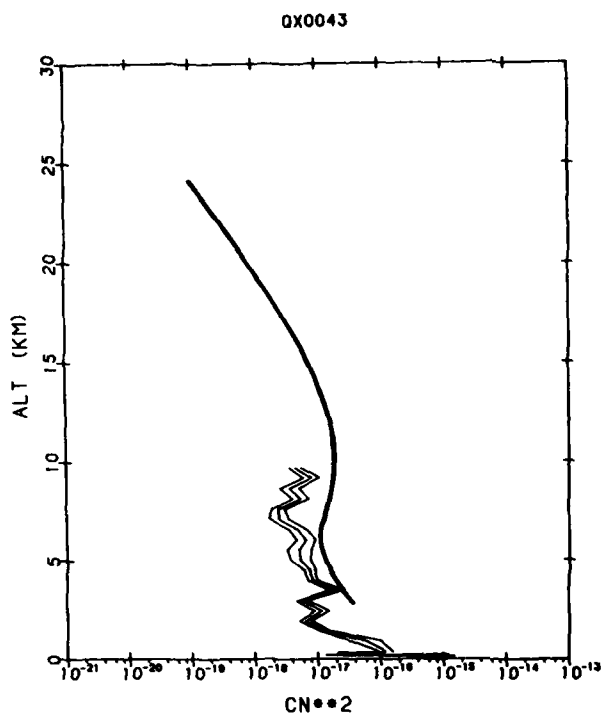


Figure 45. Log-Average C_n^2 Thermosonde Profiles and the Hufnagel Model - Flight QX0043. Launched at 2141Z on 29 July 1983. Thermosonde values were averaged every 500 m, and curves showing the mean multiplied by, and divided by, 1 sigma values are shown on either side of the mean. The thick line shows the C_n^2 values from the Hufnagel model

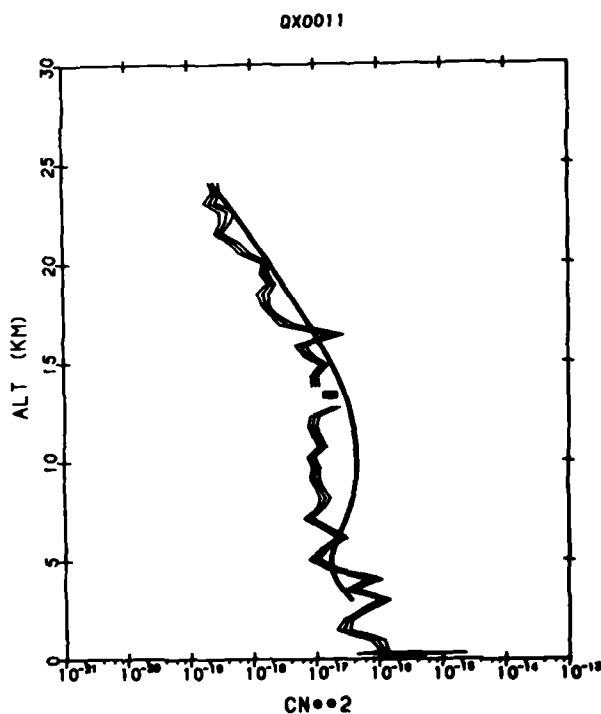


Figure 46. Log-Average C_n^2 Thermosonde Profiles and the Hufnagel Model - Flight QX0011. Launched at 0113Z on 30 July 1983. Thermosonde values were averaged every 500 m, and curves showing the mean multiplied by, and divided by, 1 sigma values are shown on either side of the mean. The thick line shows the C_n^2 values from the Hufnagel model

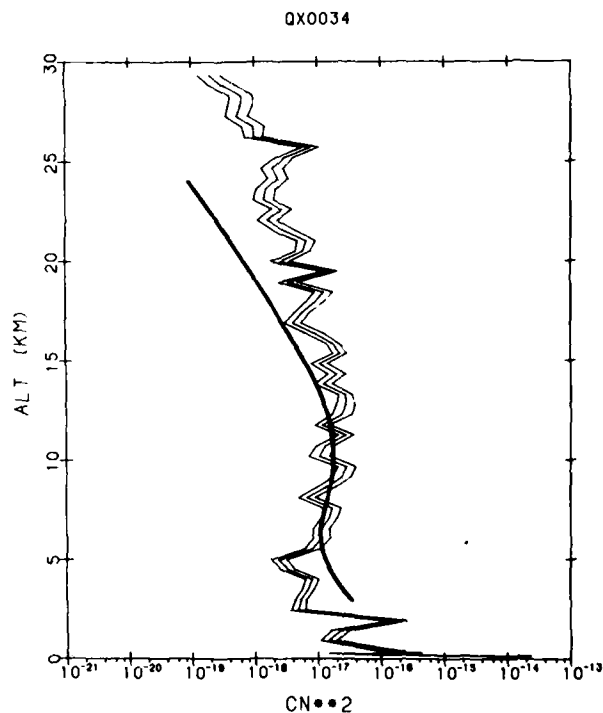


Figure 47. Log-Average C_n^2 Thermosonde Profiles and the Hufnagel Model - Flight QX0034. Launched at 2016Z on 30 July 1983. Thermosonde values were averaged every 500 m, and curves showing the mean multiplied by, and divided by, 1 sigma values are shown on either side of the mean. The thick line shows the C_n^2 values from the Hufnagel model

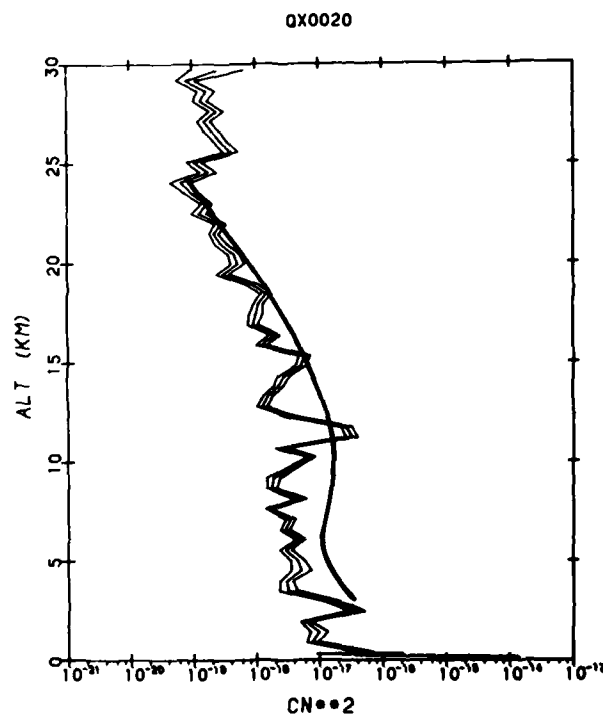


Figure 48. Log-Average C_n^2 Thermosonde Profiles and the Hufnagel Model - Flight QX0020. Launched at 0128Z on 31 July 1983. Thermosonde values were averaged every 500 m, and curves showing the mean multiplied by, and divided by, 1 sigma values are shown on either side of the mean. The thick line shows the C_n^2 values from the Hufnagel model

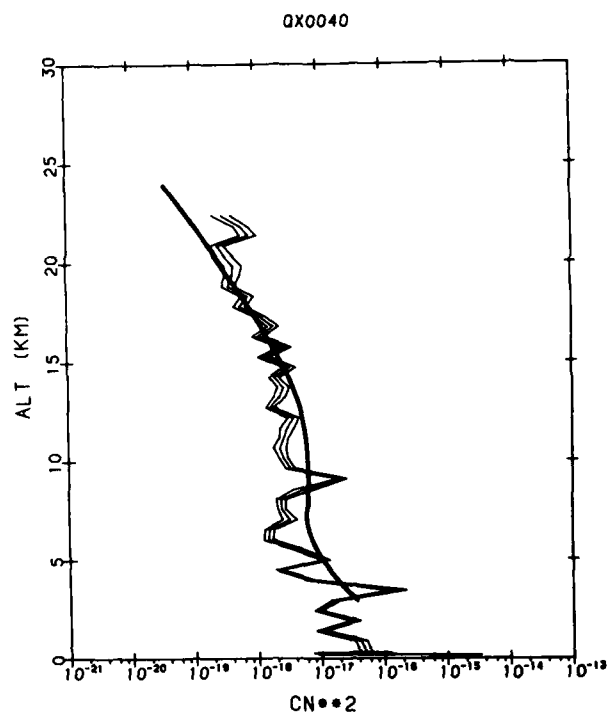


Figure 49. Log-Average C_n^2 Thermosonde Profiles and the Hufnagel Model - Flight QX0040. Launched at 0331Z on 7 Aug 1983. Thermosonde values were averaged every 500 m, and curves showing the mean multiplied by, and divided by, 1 sigma values are shown on either side of the mean. The thick line shows the C_n^2 values from the Hufnagel model

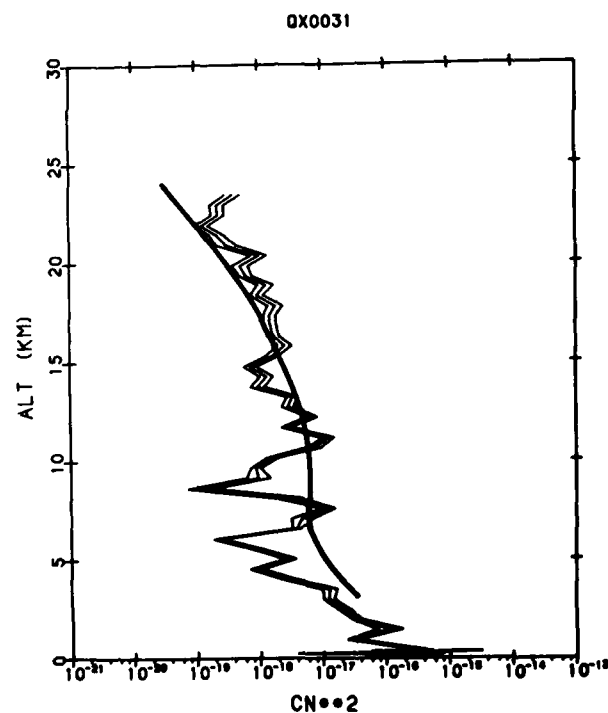


Figure 50. Log-Average C_n^2 Thermosonde Profiles and the Hufnagel Model - Flight QX0031. Launched at 0550Z on 8 Aug 1983. Thermosonde values were averaged every 500 m, and curves showing the mean multiplied by, and divided by, 1 sigma values are shown on either side of the mean. The thick line shows the C_n^2 values from the Hufnagel model

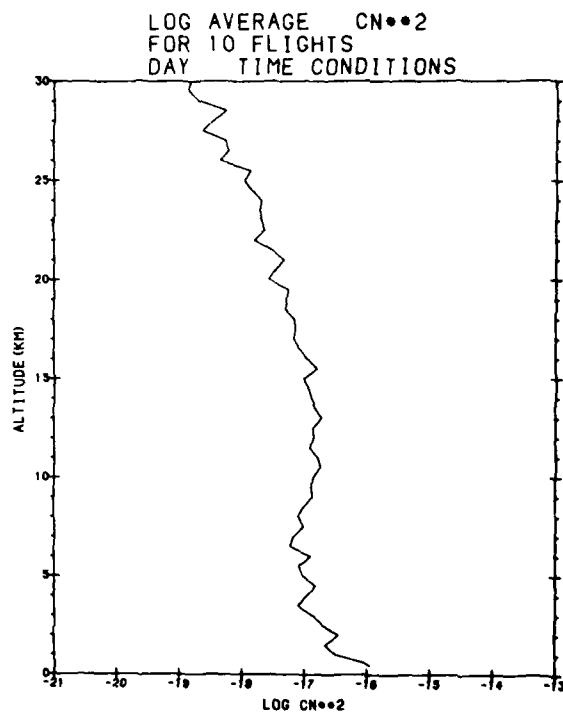


Figure 51. Log-Average C_n^2
of Ten Daytime Thermosonde
Flights

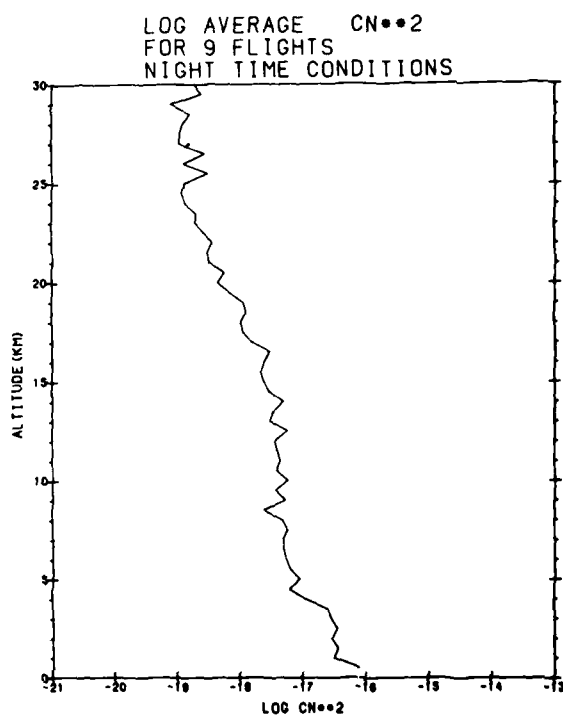


Figure 52. Log-Average C_n^2
of Nine Nighttime Thermosonde
Flights

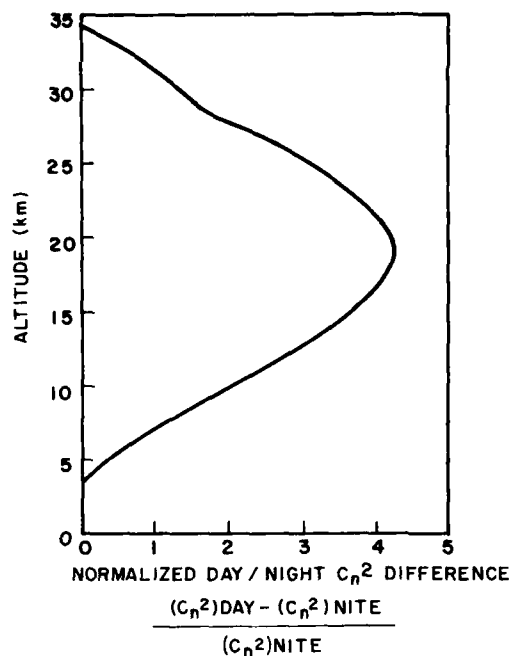


Figure 53. Normalized Difference Between Day and Night Measurements of $C_n^2 \equiv \frac{\text{Day-Night}}{\text{Night}}$

5. THERMOSONDE - RADAR COMPARISON

For those flights where radar C_n^2 data exists, composite radar C_n^2 profiles were constructed by assembling the data in 500-m bins. It was desired to compare the radar data with the 500-m log averaged thermosonde data as closely as possible in time and space. Since the log-average thermosonde data is centered at known times and altitudes, radar data could be placed into altitude bins corresponding to the balloon time ± 250 sec and altitude ± 250 m. This being done, the data in each bin were log-averaged and resulted in those profiles shown in Figures 54-61. Since each individual raw radar profile was provided for each minute of flight, the points on the graphs are log-averages of about 9 radar C_n^2 values. However, due to changes in the balloon ascent rate and other factors, the actual number of points varies between 5 and 12.

Considering the difference in resolution between the two data sets and the remaining separation in horizontal position between the measurements, the agreement is good. Figure 62 shows plots of the mean differences between the radar and thermosonde turbulence for six combined flights. Generally, on average, the radar measures larger C_n^2 by about 1.2 to 2.0 times the thermosonde C_n^2 .

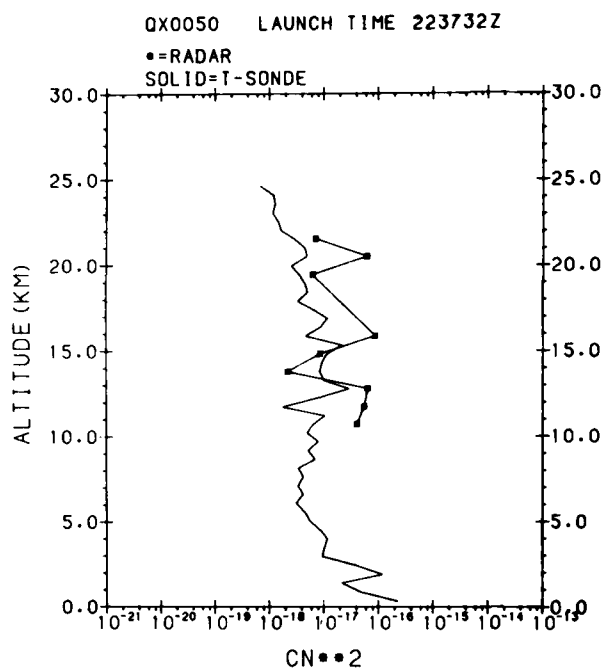


Figure 54. Comparison of 500-m Log-Average Thermosonde Profiles and Composite Log-Average Radar Profiles - Flight QX0050. Launched at 2238Z on 30 June 1983

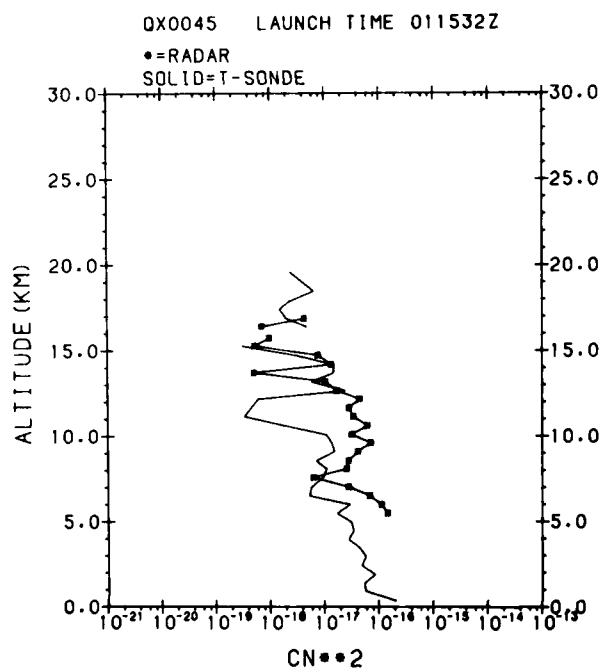


Figure 55. Comparison of 500-m Log-Average Thermosonde Profiles and Composite Log-Average Radar Profiles - Flight QX0045. Launched at 0116Z on 12 July 1983

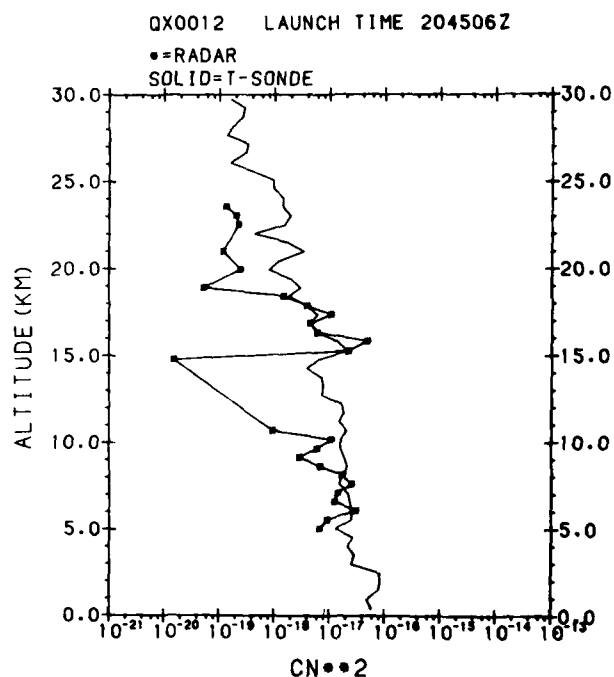


Figure 56. Comparison of 500-m Log-Average Thermosonde Profiles and Composite Log-Average Radar Profiles - Flight QX0012. Launched at 2045Z on 23 July 1983

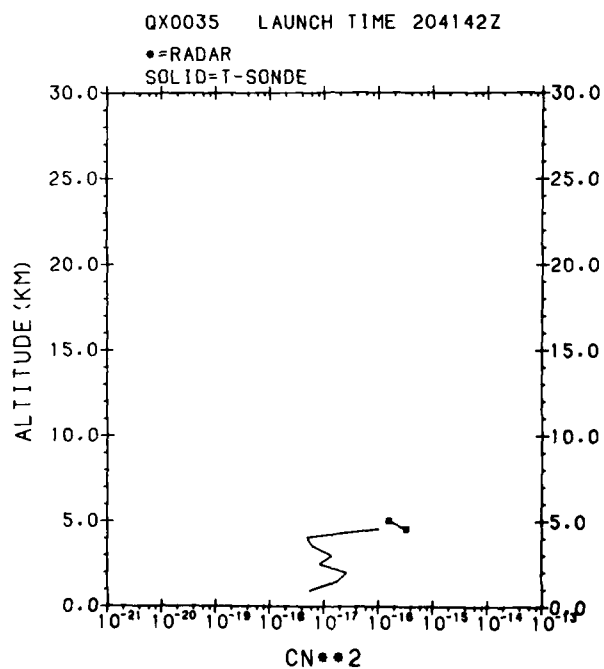


Figure 57. Comparison of 500-m Log-Average Thermosonde Profiles and Composite Log-Average Radar Profiles - Flight QX0035. Launched at 2042Z on 28 July 1983

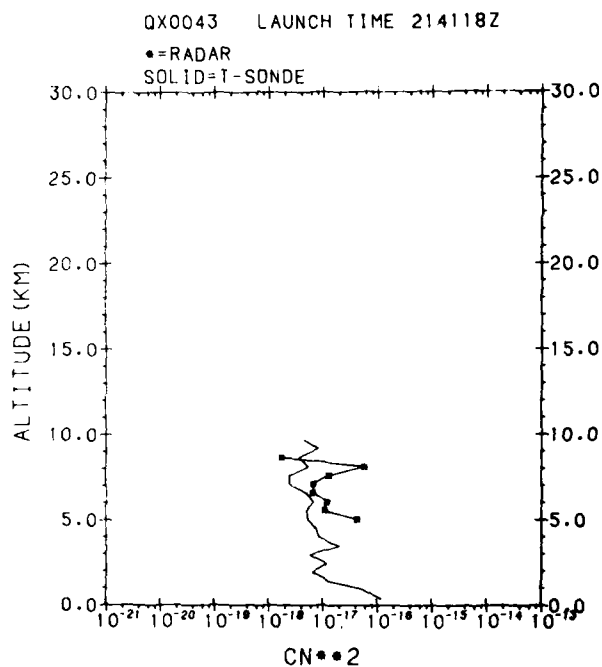


Figure 58. Comparison of 500-m Log-Average Thermosonde Profiles and Composite Log-Average Radar Profiles - Flight QX0043. Launched at 2141Z on 29 July 1983

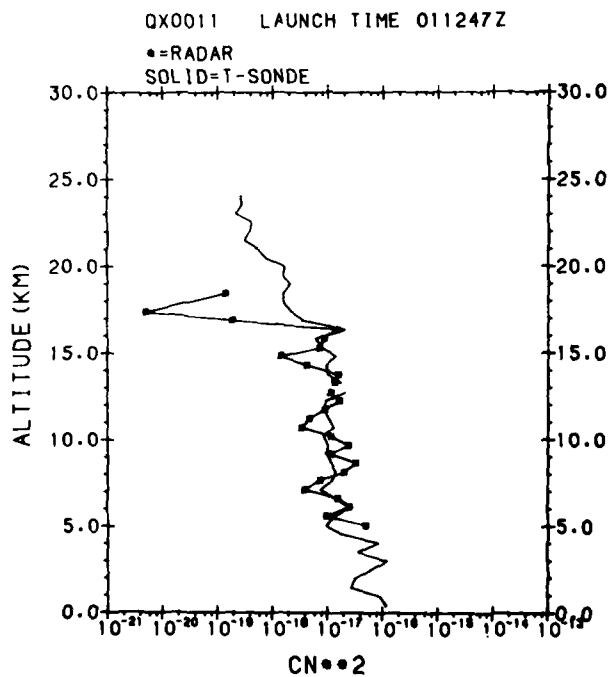


Figure 59. Comparison of 500-m Log-Average Thermosonde Profiles and Composite Log-Average Radar Profiles - Flight QX0011. Launched at 0113Z on 30 July 1983

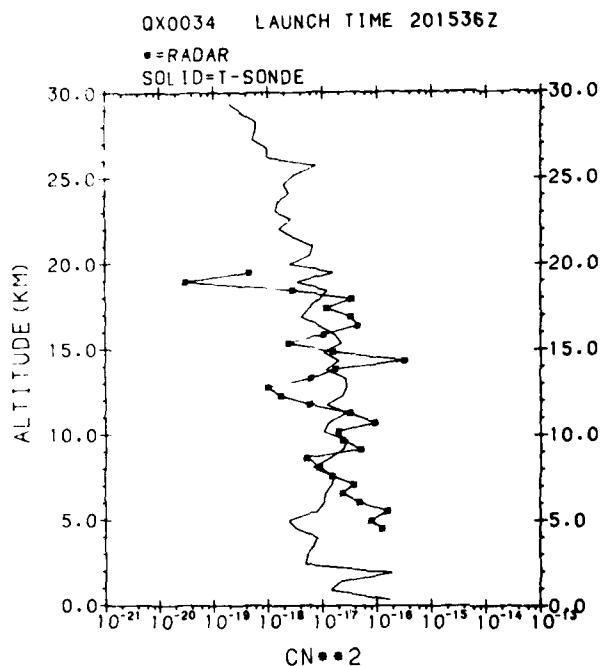


Figure 60. Comparison of 500-m Log-Average Thermosonde Profiles and Composite Log-Average Radar Profiles - Flight QX0034. Launched at 2016Z on 30 July 1983

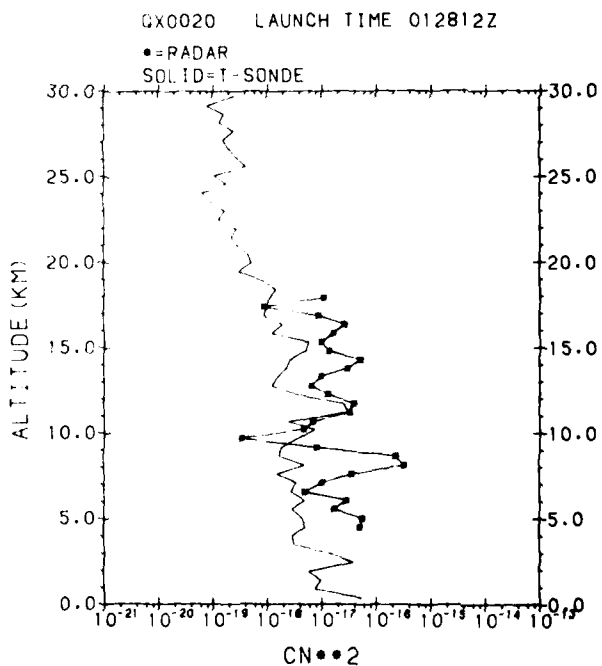


Figure 61. Comparison of 500-m Log-Average Thermosonde Profiles and Composite Log-Average Radar Profiles - Flight GX0020. Launched at 0128Z on 31 July 1983

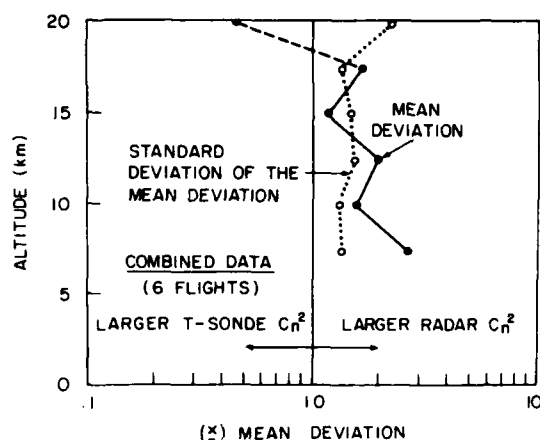


Figure 62. Plot of Mean Differences Between Thermosonde and Radar C_n^2

6. THERMOSONDE - RADAR - SCINTILLOMETER COMPARISON

On the evening of 30 July 1981, the thermosonde (QX0020), radar, and scintillometer operated together successfully. Results of their C_n^2 measurements are shown in Figure 63. The thermosonde profile, shown by the thin line, starts 0.5 km above the surface and ends at 30 km. This is a 500-m weighted log-average of the data. The radar profile, shown by asterisks, is a time/altitude weighted log-average composite of the data. It tends to match radar time and altitude with the balloon trajectory, though not in the horizontal plane. The scintillometer profile, shown by the thick line, was observed at 0208 h UT when the balloon was at 12.5 km. Over a 1-h time period, the maximum excursion of the scintillometer C_n^2 data at any one altitude was approximately 1 order of magnitude.³ The trend line of the thermosonde profile coarsely agrees with this one scintillometer profile, but until additional comparisons are made only the suggestion of agreement is postulated. More extensive thermosonde/scintillometer comparisons were conducted in March 1983 in Boulder, Colorado. These will be reported in a future report.

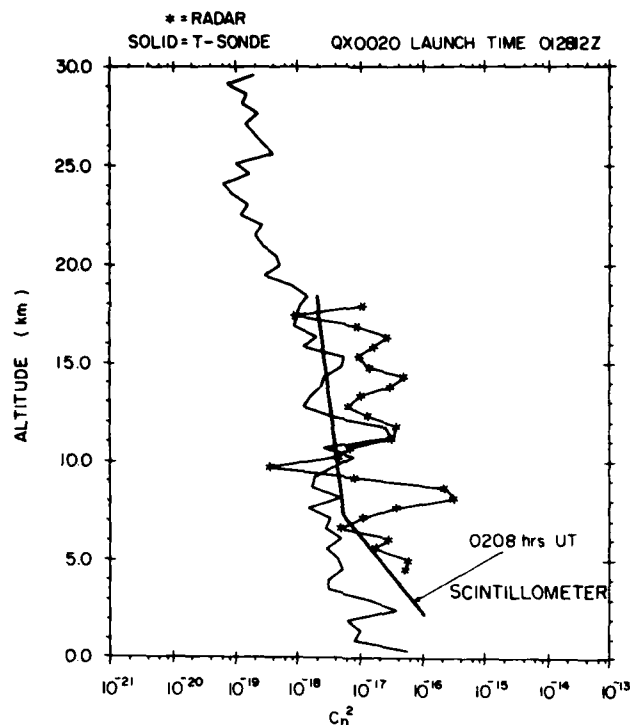


Figure 63. Comparisons Between Log-Average Thermosonde, Radar, and Scintillometer C_n^2 Profiles - One Flight

7. THERMOSONDE - AIRCRAFT COMPARISON

Hot wire anemometer C_n^2 experiments were conducted from the ARA airplane on 11 July 1981 and 16 July 1981. Thermosonde and airplane experiments were conducted together successfully on the night of 11 July. The thermosonde launch was at 0115 h UT while the aircraft took measurements from 0133 to 0247 h UT. Measurements were taken during ascent to 8.5 km and then during descent to 0.5 km. The resulting profiles are compared to the thermosonde measurements in Figures 64-67. Two separate bridge circuits measured aircraft C_n^2 data independently. Bridge No. 1 measured C_n^2 values about 2 to 4 times that of the thermosonde except for the lowest altitude descent data. Bridge No. 2 was high by an order of magnitude and was not correctly calibrated. Further evidence of aircraft measurement error was seen in comparative measurements of 27 Dec 1983 and 30 Dec 1983 where the aircraft showed 1 to 2 orders of magnitude higher C_n^2 . Clearly, the ARA aircraft measurements produce gross error. This technique is not recommended for future programs unless more study produces better information on the sources of the error.

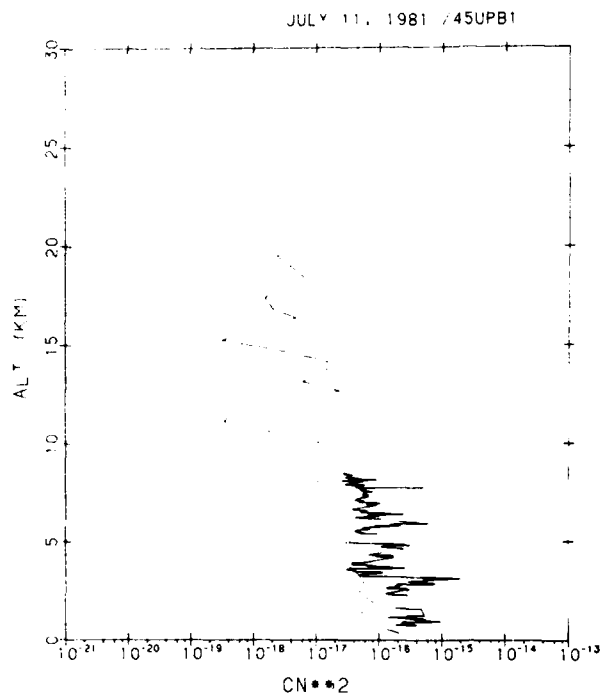


Figure 64. Thermosonde -
Aircraft Profile
(Ascent, Bridge No. 1)

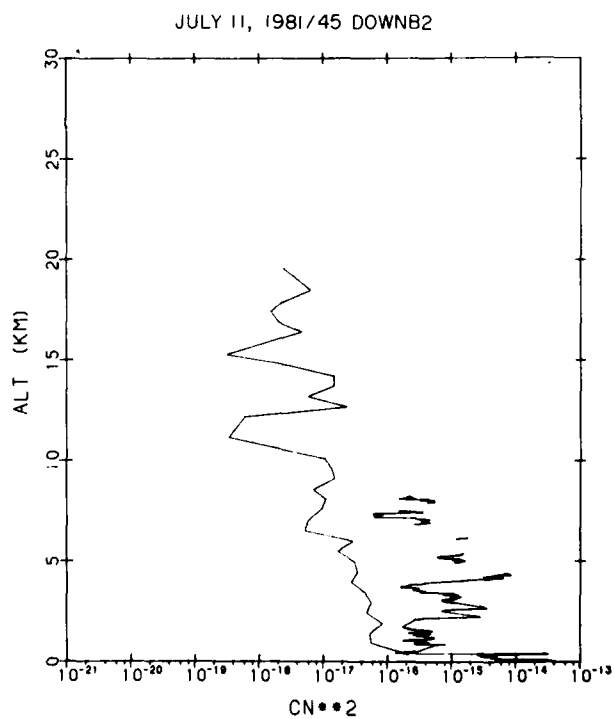


Figure 65. Thermosonde -
Aircraft Profile
(Descent, Bridge No. 1)

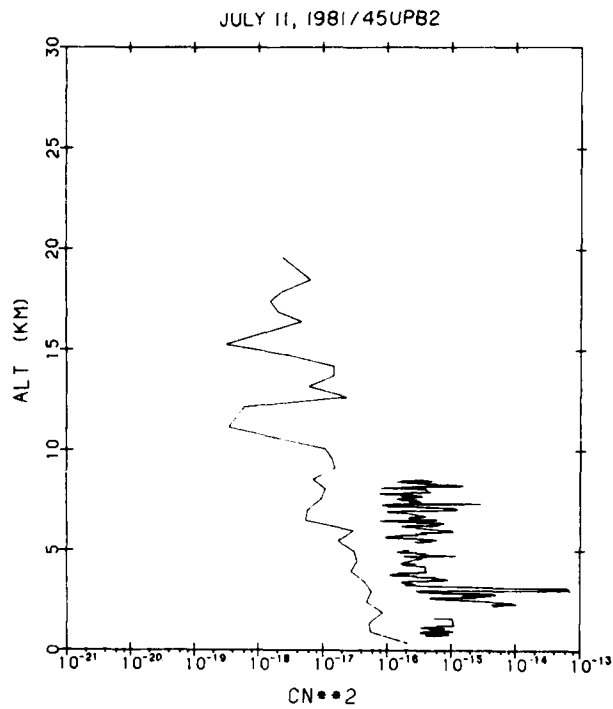


Figure 66. Thermosonde -
Aircraft Profile
(Ascent, Bridge No. 2)

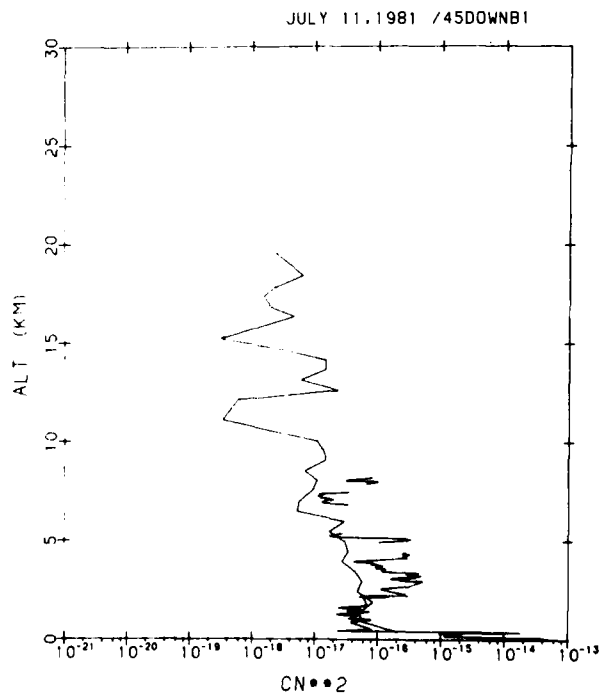


Figure 67. Thermosonde -
Aircraft Profile
(Descent, Bridge No. 2)

References

1. Brown, J.H., Good, R.E., Bench, P.M., and Faucher, G.E. (1982) Sonde Experiments for Comparative Measurements of Optical Turbulence, AFGL-TR-82-0079, AD A118740.
2. Tatarski, V.I. (1961) Wave Propagation in a Turbulent Medium, McGraw-Hill Co., New York.
3. Good, R.E., Watkins, B.J., Quesada, A.F., Brown, J.H., and Lorient, G.B. (1982) Radar and optical measurements of C_n^2 . Appl. Opt., 21:3373-3376.
4. Ottersten, H.H. (1969) Radar backscattering from the turbulent clear atmosphere, Radio Science, 4:1251-1255.
5. Balsley, B.B., and Gage, K.S. (1980) The MST radar technique: potential for middle atmospheric studies, Pure Appl. Geophys., 118:452.
6. Ochs, G.R., Wang, T., Lawrence, R.S., and Clifford, S.F. (1976) Refractive-turbulence profiles measured by one-dimensional spatial filtering of scintillations, Appl. Opt., 15:2564-2510.
7. Fairall, C.W., and Markson, R. (1979) Aircraft Measurements of Micro-Meteorological Parameters at Panama City, Florida in 1978, Naval Post-graduate School Technical report.
8. Hufnagel, R.E. (1974) Variations of atmospheric turbulence, The Infrared Handbook, USGPO, Washington, D.C., Chapter 6, pp 1-56.
9. Van Zandt, T.E., Gage, K.S., and Warnock, J.M. (1981) An Improved Model for the Calculation of Profiles of C_n^2 and ϵ in the Free Atmosphere from Background Profiles of Wind, Temperature and Humidity, 20th Conference Radar Meteor. Soc., Boston, Amer. Met. Soc., pp 129-135.
10. Fried, D.L. (1966) Optical resolution through a randomly inhomogeneous medium for very long and very short exposures, J. Opt. Soc. Am., 56:1372-1379.
11. Walters, D.L., Favier, D.L., and Hines, J.R. (1979) Vertical path measurements MTF measurements, J. Opt. Soc. Am., 69:828-837.

Appendix A

Solar Heating Effects on Probe Wire

To determine the extent of possible thermosonde measurement error due to solar heating of the probe wires, the following heat transfer analysis is suggested. External solar heating of the wire is seen to occur by direct solar radiative heating, E_{SD} , by solar radiative reflection of the atmosphere, E_{SR} , and by long wave radiation from the earth, E_{LE} . Probe cooling is seen to occur by long wave radiation from the wire E_{LW} , and by convective cooling, E_c .

Estimates of the heat transport are obtained from the following:

$$E_{SD} = \frac{f S \epsilon_T A_s}{F_D}$$

where

f = estimate of fraction of solar radiation reaching a given altitude

$f \approx 0.5$ at surface

$f \approx 0.9$ at 30 km

S = solar constant = 0.14 W cm^{-2}

A_s = surface area of wire $2\pi RL$

ϵ_T = estimate of wire absorbitivity for visible wavelength ≈ 0.4

F_D = form factor for direct radiation = π

$$E_{SR} = \frac{f S \epsilon_T \alpha A_s}{F_R}$$

where

α = estimate of fraction of reflected radiation ≈ 0.35

F_R = form factor for reflected radiation = 2.0

$$E_{LE} = \frac{S_e \epsilon_{LW} A_s}{F_R}$$

where

S_e = estimate of heat flux from earth at a given altitude

$S_e \approx 0.066 \text{ W cm}^{-2}$ at surface

$S_e \approx 0.022 \text{ W cm}^{-2}$ at 30 km

ϵ_{LW} = estimate of wire emissivity for long wave radiation ≈ 0.03

$$E_{LW} = \epsilon_{LW} A_s \sigma T_s^4 \approx \epsilon_{LW} A_s \sigma [T_e^4 + 4 \Delta T T_e^3]$$

where

σ = Stephan-Boltzman constant = $5.67 \times 10^{-12} \text{ W cm}^{-2} \text{ K}^{-4}$

T_s = wire temperature, K

T_e = air temperature, K $\approx 300 \text{ K}$ at surface and 225 K at 30 km

$\Delta T = (T_s - T_e)$

$T_s^4 \approx [T_e + 4 \Delta T T_e^3]$ for $\Delta T \ll T_e$

$$E_c = J A_s h \Delta T$$

where

J = mechanical equivalent of heat = 4.18 W/cal/s

h = estimate of convective heat transfer coefficient

$h \approx 0.12 \text{ cal cm}^{-2} \text{ sec}^{-1} \text{ K}^{-1}$ at surface

$h \approx 0.031 \text{ cal cm}^{-2} \text{ sec}^{-1} \text{ K}^{-1}$ at 30 km.

Now since, $E_{SD} + E_{SR} + E_{LE} = E_{LW} + E_c$ and combining terms,

$$\Delta T = \frac{1}{Jh} \left\{ fS \epsilon_T \left(\frac{1}{F_D} + \frac{\alpha}{F_R} \right) + \epsilon_{LW} \left(\frac{S_e}{F_R} - \alpha T_e^4 \right) \right\}$$

for daytime conditions,

$$\begin{aligned} \Delta T &= 0.03 \text{ deg at surface} \\ &= 0.19 \text{ deg at 30 km} \end{aligned}$$

for nighttime conditions, the solar radiative term vanishes, and

$$\Delta T \approx 0.$$

The conclusions are of course that we need not be concerned with nighttime heating. Daytime solar heating will not raise the wire temperature more than 0.03 deg and 0.2 deg above ambient conditions at the surface and 30 km respectively. Since this is a dc effect upon both wires, the ac bridge will remove the gross imbalance, if any. Small velocity fluctuations in the air flow over the wires can cause small variations in the heat transfer coefficient, especially at the surface. A large fluctuation in windspeed, say 10 percent, can cause at most a 10 percent change in the heat transfer coefficient. This will produce, at most, an ac temperature fluctuation of 0.003° C, an undetectable fluctuation. The velocity effect on the heat transfer coefficient *falls off* rapidly with altitude. At 10 km, a 10 percent velocity fluctuation can cause very little temperature fluctuation. At 30 km, no change in the heat transfer coefficient will be caused by forced convection and hence no detectable temperature fluctuation will be produced.